CFD-Based Optimization of

Electrothermal Rotor Ice Protection Systems

Adam Targui

Department of Mechanical Engineering

McGill University, Montreal

December 2020

A thesis submitted to McGill University in partial fulfillment of the requirements of the degree

of Master of Engineering

Abstract

Rotorcraft fly mission profiles which occasionally put them at risk of exposure to in-flight icing conditions, a hazardous phenomenon that can lead to departure from controlled flight. The helicopter rotor is responsible for lift generation and control along the pitch and roll axes and is therefore an essential component to protect against ice accretion. Ice protection systems (IPS) used in helicopters differ from that of aircraft due to the smaller wing cross-section and the lower onboard power available. Electro-thermal heating pads are a prevalent solution answering these constraints, as they are thin and can fully conform to a blade profile. Current research to optimize electro-thermal IPS is limited to airfoils, while flows and icing on aircraft wings and helicopter rotors are highly three-dimensional in nature. The present methodology proposes a 3D IPS optimization framework for electro-thermal anti-icing IPS of rotorcraft in hover and forward flight.

The governing physics are those of a conjugate heat transfer (CHT) problem between a fluid and a solid domain. Therefore, simulation results are provided by the FENSAP-ICE system, augmented with an array of compatible tools for rotorcraft simulation. Furthermore, Reduced Order Modeling (ROM) is used to limit the computational cost of returning an objective function or constraint evaluation to the optimizer at every iteration. The derivative-free optimization software package NOMAD is employed in this study.

The framework seeks to optimize the design variables of heating pads extent and power usage. The tool also aims to be versatile by addressing several optimization formulations while remaining computationally efficient.

Résumé

Les aéronefs à voilure tournante ont des missions qui les exposent occasionnellement au risque de givrage en vol, un phénomène qui peut devenir catastrophique s'il n'est pas contrôlé. Le rotor principal d'un hélicoptère est responsable de la génération de la portance ainsi que du contrôle des axes de tangage et de roulis, et il est donc critique de protéger ce composant du givrage. Les systèmes de protection contre le givrage utilisés par les hélicoptères diffèrent de ceux des avions à voilure fixe dû au volume interne restreint des pales ainsi que de la puissance limitée des moteurs d'hélicoptères. Les systèmes de protection électrothermiques sont favorisés par ces contraintes puisqu'ils sont minces et peuvent être adaptés au profil des pales. Présentement, la recherche dans le domaine de l'optimisation des systèmes électrothermiques est limitée aux profils aérodynamiques bidimensionnels alors que l'écoulement et le givrage sur les rotors sont tridimensionnels. La méthodologie présentée propose un outil tridimensionnel d'optimisation des systèmes d'antigivrage électrothermiques aux rotors d'aéronefs à voilure tournante en vol avant et stationnaire.

La physique du problème est celle d'un transfert de chaleur conjugué entre air et solide. Les simulations numériques sont effectuées par le logiciel FENSAP-ICE, augmenté par des outils adaptés aux giravions. De plus, l'utilisation de modèles réduits diminue le temps nécessaire à l'évaluation de la fonction à optimiser et des contraintes à chaque itération. À cette fin, l'optimiseur sans dérivées NOMAD est utilisé dans cette thèse.

Le cadre développé cherche à optimiser les variables de la distribution et de la puissance des plaques chauffantes. L'outil comprend aussi l'objectif d'être polyvalent en offrant la capacité

de résoudre diverses formulations du problème d'optimisation tout en limitant les coûts calculatoires.

Acknowledgments

First, I extend my sincere gratitude to my primary thesis supervisor Professor Wagdi G. Habashi for his mentorship, guidance and transmission of a wealth of knowledge about aero-icing, rotorcraft, turbomachinery and aerospace in general. My research experience at the McGill CFD Lab under his supervision is an honor and privilege that I deeply appreciate.

I thank all my fellow colleagues for making work at the Lab a pleasure. A special thanks goes to Dr. Vincent Casseau, post-doctoral fellow at the CFD Lab, who tirelessly addressed my queries, provided continuous feedback and ensured the smooth advancement of my project.

I wish to thank Dr. Song Gao and Mr. Shezad Nilamdeen from ANSYS Canada, both graduates of the McGill CFD Lab, for their continuous help and eagerness to respond to any issues that I raised during my research. Financial support for my project was provided by the NSERC-Lockheed Martin-Bell Helicopter Industrial Research Chair, I thank you for enabling my research. I also extend to Calcul Quebec my appreciation for the computational resources which complemented the CFD Lab's to help expedite my numerical simulations.

I thank the members of the Montreal aerospace community in both the industry and academia for providing unforgettable opportunities, formative experiences, first-hand knowledge and unparalleled expertise to contribute to my personal growth. You have continuously inspired me to remain passionate about the field.

Finally, I thank my friends and family for their unwavering support throughout my journey.

Dedication

This thesis is dedicated to my parents for their unconditional support. I am forever grateful.

Table of Contents

List of Figures

List of Tables

Nomenclature

$\boldsymbol{A}$ = Matrix of snapshots

$\boldsymbol{c}$ = Optimization constraints

c_h = convective heat transfer coefficient

c_p = specific heat capacity

C_d = droplets drag coefficient

$\boldsymbol{D}$ = Mesh directions set

E = Internal energy

$\boldsymbol{f}$ = Objective function

Fr = Froude number

$\boldsymbol{g}$ = Gravity vector

h_f = Water film height

H = Enthalpy

K = Droplet inertial parameter

L = Latent heat

Li = Concentrated log-likelihood function

m = POD modes

$\dot{m}$ = mass flow rate

$\boldsymbol{M}$ = Mesh set

N_D = Number of design variables

N_P = Number of data points per snapshot

N_S = Number of snapshots

$\boldsymbol{p}$ = Optimization parameters

$\boldsymbol{P}$ = Poll trial points set

p = Static pressure

Q = Heat flux

$\boldsymbol{r}$ = Correlation vector

$\boldsymbol{R}$ = Correlation matrix

Re = Reynolds number

T = Temperature

$\boldsymbol{U}$ = Snapshot

$\boldsymbol{V}$ = Velocity vector

v = Velocity component

$\boldsymbol{x}$ = Design variables vector

$\boldsymbol{y}$ = Observed function values vector

$\hat{y}$ = Kriging predictor

Y = Random variable

Greek Letters

α = Water volume fraction

β = Water collection efficiency

γ = Kriging's mean term

Δ_m = Mesh size parameter

Δ_p = Poll size parameter

ζ = POD eigenfunction

$\boldsymbol{\theta}$ = Weight parameter

κ = Thermal conductivity

Λ = POD eigenvalue

μ = Dynamic viscosity

$\hat{\mu}$ = Estimated mean

ρ = Density

$\boldsymbol{\sigma}$ = Stress tensor

$\hat{\sigma}$ = Estimated covariance

τ = Shear stress

$\boldsymbol{\varphi}$ = POD basis function

ω = POD basis coefficient

Abbreviations

AERTS: Adverse Environment Rotor Test Stand

CHT: Conjugate Heat Transfer

CFD: Computational Fluid Dynamics

CVT: Centroidal Voronoi Tessellation

DoE: Design of Experiments

ETRIPS: Electrothermal Rotor Ice Protection Systems

HT: Heater abbreviation in figures

IPS: Ice Protection Systems

LOOCV: Leave-One-Out Cross-Validation

LWC: Liquid Water Content

MVD: Median Volumetric Diameter

NOMAD: Nonlinear Optimization by Mesh Adaptive Direct Search

OAT: Outside Air Temperature

POD: Proper Orthogonal Decomposition

RANS: Reynolds-Averaged Navier-Stokes

ROM: Reduced Order Modeling

Subscripts

a = air

d = droplet

δ = untried location

f = fluid

s = surface

w = water

∞ = freestream

1 Introduction

1.1 Research motivation

Unmitigated ice accretion on key aerodynamic surfaces can lead to lack of controlled flight for an aircraft. Helicopters are more susceptible to icing than their equivalent fixed-wing counterparts because of mission profiles leading them to operate at low altitudes. Tasked with lift generation and control along the pitch and roll axes, the helicopter rotor is therefore a critical component to protect against icing. Helicopter IPS must cope with smaller wing cross-sections and lower onboard power available compared to fixed-wing aircraft, posing additional design challenges for optimization of the IPS. Electrothermal heating pads are thus more often used as they are slender and capable of conforming to a rotor blade profile. Located in critical areas and regulated individually by an electrical circuit, they allow a tailored and quick response to changing icing conditions.

The McGill CFD Lab's framework for rotorcraft simulation provides high-fidelity three-dimensional flow computation capabilities. It offers a palette of CFD-based tools tackling aerodynamics, structures, ice accretion, shedding and tracking, as well as a stitching module addressing a wide range of rotorcraft configurations, including rotor-fuselage interactions or the case of multiple rotors. The array of tools is coupled to FENSAP-ICE, a software developed at the McGill CFD Lab [1] and currently distributed commercially by ANSYS. FENSAP-ICE is a finite element-based modular solver for flow, droplet impingement, icing, solid domain conduction and includes a dedicated CHT module. Therefore, the existing mature framework paves the way for more advanced IPS simulation capabilities for rotors which this thesis is concerned with.

Furthermore, the feasibility of interfacing FENSAP-ICE with optimization tools is proven by the existence of a previously developed two-dimensional framework for IPS optimization within the McGill CFD Lab. Expected challenges related to high computational costs associated with CFD optimization can be addressed with the use of the McGill CFD Lab's dedicated ROM module. As such, the addition of IPS optimization to the existing framework's flow, ice accretion, ice shedding and fluid-structure interaction capabilities is a natural continuation of current research in the quest for a comprehensive rotorcraft analysis tool.

1.2 Thesis outline and contributions

The present work seeks to create an IPS optimization framework for three-dimensional wings, as well as rotorcraft in hover and forward flight. The proposed framework combines multi-physics solvers, ROM and an optimizer. The framework is versatile, allowing users to address different optimization problem formulations by offering a variety of objective functions, parameters and constraints. It is also cost-effective, aimed at assisting the design of the IPS for helicopters. The framework developed creates an automated IPS optimization process. First, the tool automatically generates CFD snapshots by translating sets of design variables obtained from a design of experiments (DoE) module into flow, icing and CHT runs. As such, based on initial user templates for the simulations and the solid domain mesh, the framework creates new heating zones, edits FENSAP-ICE configuration files and executes all the CFD computations. Then, the framework post-processes the CFD solutions to extract the constraint and objective functions and uses a ROM module to create a metamodel. Finally, the tool performs ROM-optimizer interfacing by passing design variables as well as constraint and objective functions between both packages.

The thesis is organized as follows: first, a literature review is conducted and followed by a general problem formulation with the methodologies used to perform CHT computations and ROM-based optimization. Then, results for various optimization problems are shown, error analyses are conducted and, finally, conclusions are drawn.

2 Background & literature review

2.1 Aircraft IPS

Several types of IPS are used with varying prevalence on airplanes and rotorcraft. Hot-air, mechanical, chemical, passive and electrothermal systems are the five main categories of onboard anti-icing and de-icing solutions utilized.

Large commercial airplanes are generally equipped with hot-air systems, where bleed air is routed to protect critical surfaces from icing. These include the nacelles and the wings' leading edge, where piccolo tubes force streams of hot air along the inner surface. The impinging jets heat the inner walls, conduction through the surface then occurs to reach the external iced wall. However, such systems necessitate a high bleed air output, mechanical complexity and available volume within the component to be protected. Therefore, it would be infeasible to implement hot-air IPS on a slender rotating rotor blade powered by a turboshaft engine [2].

Mechanical ice protection systems seek to break and shed built-up ice by deforming the surface experiencing ice accretion. Several variations of this system exist and are primarily used to de-ice the leading edge of wings, engine inlets, propellers as well as horizontal and vertical stabilizers. The most common type, pneumatic de-icing systems, use bleed air to inflate a membrane and cause the deformation of the leading edge. First introduced by Goodrich in 1933 [3], they are ubiquitous in turboprop aircraft as they are lightweight, easy to maintain and require less energy than hot-air systems. However, to ensure shedding, a minimum ice buildup is required prior to activation. Furthermore, this IPS is often limited to the leading edge, risking accumulation of unshed and re-frozen ice aft of the protected extent. With turboprops having limited onboard bleed air, some designs may not allow for all aircraft sections to be de-iced simultaneously, but sequentially, increasing the vulnerability of the aircraft. More modern electro-mechanical systems use electrical currents to induce magnetic fields that cause the metallic aerodynamic surface to displace. Examples include electro-impulse de-icing (EIDI) [4] and electro-magnetic expulsion de-icing system (EMEDS) [5] systems. However, within the realm of rotorcraft, early investigative effort into anti-icing and de-icing methods led by Lockheed in 1973 [2] have discounted mechanical IPS at the conceptual stage. Among other factors, the required bleed air amount remained prohibitively high, the slender profile and small leading-edge rotor radii raised effectiveness and integration issues while extreme centrifugal forces were deemed to threaten the structural integrity of de-icing boots. Although research in the field continues and experimental integration attempts on rotors are made with new systems that break accreted ice with ultrasonic waves [6] as well as traditional pneumatic systems [7], no operational helicopter rotor utilizes mechanical IPS.

Chemical systems fall under a category where no thermal heating nor geometry change of the aerodynamic surface is used to mitigate ice accretion. Instead, ice formation is inhibited by continuously delivering a freezing point depressant such as glycol to the protected surface. Similarly, de-icing solutions can also be pumped to chemically break the bond between the ice and the surface. Developed in the 1940s, these weeping-wing systems are still in use today mostly in general aviation [5]. While more energy efficient than bleed air and electrothermal IPS, only a finite reservoir of onboard fluid is available and the necessity of replenishing its supply between flights restricts the adoption of chemical systems. Furthermore, very limited success has been achieved during the testing of chemical IPS on helicopter rotors due to difficulties arising from uneven fluid distribution over the rotor span [8].

Passive systems utilize ice-phobic surface coatings to reduce the adhesion of the ice to the surface [9]. While necessitating no energy and being the subject of ongoing research, their limited durability and resistance to erosion as well as unsatisfactory performance in prolonged severe icing conditions prevent them from being used as the primary IPS [10].

Increased electric power generation capacity on modern aircraft enables the use of electrothermal systems instead of hot-air IPS on airplanes such as the Boeing 787 [11]. In the domain of rotorcraft, electrothermal systems remain the exclusive IPS for helicopter rotors [6]. While needing to draw from the limited on-board electrical power, electrothermal rotor ice protection systems (ETRIPS) are currently the only practical solution offering adequate protection for de-icing. Contrary to hot-air and pneumatic IPS, the protected zone can be designed to extend beyond the leading edge, mitigating runback and refreezing ice.

2.2 Rotorcraft ETRIPS

ETRIPS investigations have been carried out by academia and industry but experimental and numerical results focusing on their optimization are scarce within the open literature. Insightful design and experimental work has been conducted for a four-bladed 1970s Sikorsky helicopter and a two-bladed 1960s Bell aircraft. In both cases, the protected surface extends along the quasi-totality of the span of the rotor and covers the leading-edge using cyclic operations alternating between the different heating zones. The activation and operation of the de-icing system installed on each rotorcraft takes place following measurements from an ice detector and dedicated sensors of outside air temperature (OAT) and liquid water content (LWC, correlated from an icing rate meter) values. Furthermore, the de-icing cycle is automatic as the system controls on and off times of the individual heating zones depending on the detected severity of the icing conditions. Blades are symmetrically de-iced, with individual heating zones activated simultaneously on corresponding sections on both blades of the Bell model while the Sikorsky's four blades are de-iced in pairs.

These rotorcraft share a similar operating logic but their designs differ with the former's main rotor presenting a four-zone chordwise heater distribution wrapped around the leading edge, while the latter uses a six-zone spanwise distribution from root to tip. As such, the protected zone of the Bell's main rotor covers the entire span and extends to 12% of the chord of the upper surface and 29% of the bottom surface. In contrast, the Sikorsky's main rotor IPS extends from 21% to 92% in the outwardly spanwise direction and protects 12% of the upper and 17% of the lower surfaces in the chordwise direction.

In 2003, Sikorsky Aircraft subsequently published its work on the S-92 which is fitted with a new rotor whose design is very similar to their 1970s model [10]. The retained ETRIPS configuration is also comparable to their older design, hence providing a baseline in this cutting-edge research. Moreover, the authors also argue that while implementing a rotor anti-icing system would maintain the rotor's surface ice-free, the needed power remains too great to keep the runback ice in a running wet situation from refreezing. Consequently, the need for optimization of anti-icing ETRIPS is highlighted.

2.3 CFD-based optimization

In the open literature, with the exception of FENSAP-ICE, methodologies used for simulating rotorcraft flows with icing are often not fully three-dimensional and use separate flow solvers and icing codes. An example is Narducci and Kreeger [12, 13, 14] where the flow field is solved by OVERFLOW and icing is handled by a non-3D icing code, incorrectly named LEWICE3D. Thus, high-fidelity CFD packages similar to FENSAP-ICE capable of fully 3D rotorcraft flow, icing and CHT are scarce, if not totally non-existent. The only comparable package claiming all these capabilities is the commercial package Star-CCM+ [15]. However, to the author's knowledge, no open source publications can be found where STAR-CCM+ is exclusively used to simulate all of rotorcraft flow, droplet impingement, ice accretion and CHT. Thus, FENSAP-ICE, with its in-house rotorcraft tools, is adopted in this work.

Optimizing ETRIPS presents the same challenges and bottlenecks than those associated with general problems in the field of Computational Fluid Dynamics (CFD), *i.e.*, solving a nonlinear system of differential equations that are computationally intensive. In this regard, the creation of reduced order models, also referred to as metamodels, which are lower fidelity models created from a higher fidelity one (in this case, 3D CFD) and the use of appropriate optimization tools can be highly beneficial to the development of an ETRIPS design framework.

Previous efforts at optimizing IPS in the McGill CFD Lab have been dedicated to fixed-wing aircraft configurations. Pellissier *et al.* [16] used ROM for heuristics-based (genetic algorithm) optimization of a hot-air anti-icing system using a piccolo tube. Pourbagian *et al.* [17, 18] developed a framework to optimize the power density and cyclic activation of an electro-thermal IPS by using ROM in conjunction with the NOMAD [19] optimization package, that is well suited for applications such as CFD where the physical models relating design variables and objective functions are complex, highly nonlinear, without defined gradients and with their innerworkings potentially inaccessible to the user. While the application of that work was limited to wings, it lay the groundwork for this thesis by outlining the needed ROM and optimization tools to integrate in a new ETRIPS framework. Within the literature, with one exception where optimization of the internal structure of the ETRIPS heaters was sought [20], no attempt at CFD-based ETRIPS optimization has been made. These authors have used both numerical simulation and an experimental setup to study the solid domain by varying the number of heating wires, their distribution, spacing as well as the thickness of conductive and insulating layers. Objective functions numerically obtained were limited to the surface skin temperature and the surface area where ice melts. However, the experimental setup is crude, consisting of a non-rotating setup emulating a 2D case where a small-sized rotor section is placed in front of a blower inside of a refrigerated environment. Furthermore, details about the numerical study are scarce and the geometry is not provided. The authors just mention that ANSYS Workbench is used for numerical simulation and that icing results are obtained via finite element simulation. Therefore, it is unclear whether a high-fidelity 3D rotorcraft flow approach was adopted.

3 Methodology

3.1 Optimization problem

A general optimization problem statement can be formulated as follows:

$$\min_{\boldsymbol{x}} \boldsymbol{f}(\boldsymbol{x},\boldsymbol{p}) \text{ subject to } \boldsymbol{c_{eq}}(\boldsymbol{x},\boldsymbol{p}) = \boldsymbol{0}, \text{ and } \boldsymbol{c_{ineq}}(\boldsymbol{x},\boldsymbol{p}) \leq \boldsymbol{0}, \tag{3-1}$$

where the objective function $\boldsymbol{f}$ is sought to be minimized with respect to the design variables $\boldsymbol{x}$ and parameters $\boldsymbol{p}$ while being subject to constraint functions $\boldsymbol{c_{eq}}$ and $\boldsymbol{c_{ineq}}$. During an optimization run, design variables change while parameters are fixed.

The developed framework allows users to choose between several optimization problems to solve by offering a selection of objective functions. The maximum instantaneous ice accretion rate function is used to minimize icing on the overall blade surface. While arguably gauging the impact of ice, it is not a direct measurement of aerodynamic degradation. Other aerodynamic quantities provided as objective functions are the torque increase and/or lift decrease. Finally, power consumption minimization can be performed, opting to leave the icing or aerodynamic variables to be treated as constraints.

In this research, inequality constraint functions are built as

$$c_{ineq}(\boldsymbol{x},\boldsymbol{p}) = c_{evaluation}(\boldsymbol{x},\boldsymbol{p}) - c_{max}.$$

Depending on the optimization problem, maximum heating power available, maximum allowable ice growth or maximum torque rise are used as constraints c_{max} represents the maximum allowable value and is held fixed throughout an optimization run. $c_{evaluation}$ is provided to the optimizer at every iteration. For ice growth and torque constraints, it is updated from the ROM.

In the case of power constrained optimization, it is computed as the sum of the heating powers of individual heaters (calculated from design variables).

Two types of design variables $\boldsymbol{x}$ can be chosen simultaneously during the optimization of the heating pads: (a) the individual heater power and (b) the extent of the heating zone. The number of design variables for individual power optimization is equal to the number of heaters used. The extent of the heating zone is described by 4 design variables: the distance of the protected zone from the root, the tip, the chordwise protected extent on the top and the bottom surfaces of the blade.

Design parameters $\boldsymbol{p}$ describe the heater configurations and are fixed during the optimization process. Parameters available are the number of heaters and their configuration. Heaters can be distributed chordwise, spanwise or a combination of both. For the latter, a leading edge parting strip design can also be added. These are set by the user a-priori and are used by the framework to partition the heating zone in the solid domain mesh. Figure 1 is a rendering of a rotor with twenty-one independent heating zones represented by the different colours (11 visible zones). The leading edge parting strip design can be seen by the red heater.

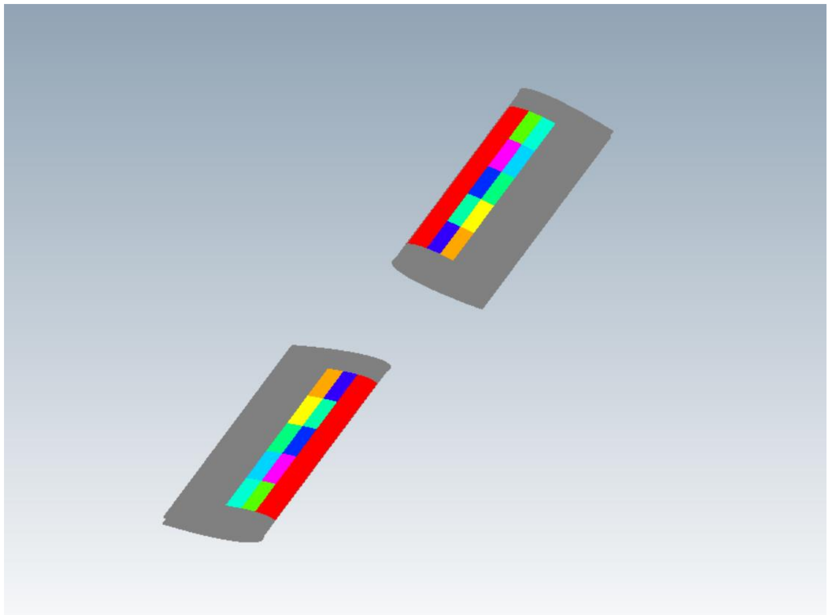

Figure 1: Illustrative example showing a combination of chordwise and spanwise heaters with a parting strip design

3.2 Conjugate heat transfer simulations

3.2.1 FENSAP-ICE

A limited selection of icing codes is available to users due to the proprietary nature of such tools. Often developed by national research entities such as NASA (LEWICE 2D and LEWICE 3D), ONERA (ONERA ICE) and CIRA (CIRA ICE), these codes remain protected and only available to their indigenous companies. However, about a decade ago, LEWICE has become commercially available. Nevertheless, it is severely limited by a cascade of simplifications of the geometry and the physics models. As such, this code belongs to panel methods as it neglects turbulence, viscosity, compressibility, and vorticity while adopting a 2D approach. In this family of methods, laminar, inviscid and incompressible flow is described by nonphysical singularities, namely sources, sinks and doublets which are numerically unstable in the limit of infinite refinement.

Instead, CFD methods discretize the continuum to apply physics-based conservation equations to describe the flow, which, in the limit of infinite mesh refinement, yield the exact solution to PDEs describing the flow. Furthermore, LEWICE is a calibrated code where agreement between ice shapes obtained from wind tunnel experiments of some airfoils and those produced by the code is enforced via the use of empirical roughness models extracted from experiments. This defeats the purpose of a predictive simulation tool for engineering design and analysis. Therefore, LEWICE is not a high-fidelity approach to complex 3D situations where flow, impingement, and ice accretion anchored in physics and not heuristics are needed.

A wide selection of numerical simulation approaches for turbulent, viscous, compressible flows exists. These include Direct Numerical Simulation (DNS), Large Eddy Simulation (LES) and Detached Eddy Simulation (DES) [21]. However, the computational cost associated with the three techniques renders them infeasible for flows over large aerodynamic bodies such as a helicopter rotor. Instead, Reynolds-Averaged Navier-Stokes (RANS) equations, augmented by a turbulence model, are used as they yield sufficiently accurate solutions for a reasonable computational cost.

As such, in the context of the CHT problem, in the fluid domain, flow solutions are obtained by solving the RANS equations to determine the convective heat flux at the fluid/solid interface. Additionally, thermal conduction originating from the heating pads passing through the blade materials affects the heat flux at the surface in the solid domain. Lastly, the energy balance at the interface must account for water content, ice accretion and phase changes due to icing [22]. High-fidelity simulation results are obtained using the FENSAP-ICE suite [1] that originated at the McGill CFD Lab. It is composed of communicating modules capable of simulating flow (FENSAP), droplet impingement (DROP3D), ice accretion (ICE3D), solid conduction (C3D) and conjugate heat transfer (CHT3D), all in three dimensions. Furthermore, for solving flows relevant to helicopter icing, the McGill CFD Lab has developed an additional arsenal of tools that include mesh deformation [23], rotor prescribed motion [24] and stitched mesh domains [25]. FENSAP-ICE has undergone extensive version control, verification, and validation to reach, by 2015, a userbase of OEMs and organizations spanning 25 countries. Furthermore, the development of its capabilities has sustained the rigors of 220 Journal and Conference publications. A cursory description of the modules' functioning is outlined next.

The Finite Element Navier-Stokes Analysis Package (FENSAP) is used to obtain all flow solutions by solving, depending on the case, steady or unsteady 3D compressible turbulent RANS. In all the results shown, turbulence is implemented following the one-equation Spalart-Allmaras model which has been extensively tested in the demanding context of aircraft icing and shown to be numerically stable and computationally efficient [26]. FENSAP executes spatial discretization by FEM and the governing equations are linearized by a Newton method. Solution time stepping is achieved by an implicit Gear scheme and iterative solving of the linear equations system is performed using a generalized minimum residual (GMRES) method. Critical for icing and CHT problems, heat fluxes at the walls are calculated by a consistent Galerkin FEM method [27] that is second-order accurate. Finally, surface roughness is not modeled heuristically but implemented via a specified sand-grain roughness calculation technique that has been shown to faithfully reproduce the evolution of roughness in time and in space until it reaches an asymptotic value [1]. This particular feature, alone, distinguishes FENSAP-ICE from other approaches that use a fixed value of roughness over the entire aircraft. Three sets of governing partial differential equations model the flow field.

For the dry-air flow (CFD Module: FENSAP), the conservation of mass is expressed by the continuity equation:

$$\frac{\partial \rho_a}{\partial t} + \nabla \cdot (\rho_a \boldsymbol{V}_a) = 0, \tag{3-2}$$

where ρ_a and $\boldsymbol{V}_a$ are respectively the density and velocity vector of air.

The momentum conservation equations are given as

$$\frac{\partial \rho_a \boldsymbol{V}_a}{\partial t} + \nabla \cdot (\rho_a \boldsymbol{V}_a \boldsymbol{V}_a) = \nabla \cdot \boldsymbol{\sigma}^{\boldsymbol{ij}} + \rho_a \boldsymbol{g}, \tag{3-3}$$

where $\boldsymbol{g}$ is the gravity vector. The stress tensor $\boldsymbol{\sigma}^{\boldsymbol{ij}}$ can be written as

$$\boldsymbol{\sigma}^{\boldsymbol{ij}} = -\delta^{ij} p_a + \mu_a \boldsymbol{\tau}^{\boldsymbol{ij}}. \tag{3-4}$$

The shear stress tensor $\boldsymbol{\tau}^{\boldsymbol{ij}}$ is expressed as

$$\boldsymbol{\tau}^{\boldsymbol{ij}} = \delta^{jk} \nabla_k v^i + \delta^{ik} \nabla_k v^j - \frac{2}{3} \delta^{ij} \nabla_k v^k. \tag{3-5}$$

The energy conservation is written as

$$\frac{\partial \rho_a E_a}{\partial t} + \nabla \cdot (\rho_a \boldsymbol{V}_a H_a) = \nabla \cdot (\kappa_a (\nabla T_a) + v_i \boldsymbol{\tau}^{\boldsymbol{ij}}) + \rho_a \boldsymbol{g} \cdot \boldsymbol{V}_a, \tag{3-6}$$

where H_a is the enthalpy, E_a is the total internal energy, T_a the static temperature and κ_a the thermal conductivity of air.

DROP3D is the droplet impingement module that uses the results of the dry-air model to calculate water impact over the 3D object. It was the first to introduce an Eulerian approach to solve droplet velocities and water volume fractions in fluid elements and is represented by the following continuity and momentum equations:

$$\frac{\partial \alpha}{\partial t} + \nabla \cdot (\alpha \boldsymbol{V}_d) = 0 \tag{3-7}$$

$$\frac{\partial \boldsymbol{V}_d}{\partial t} + \mathbf{V}_\mathrm{d} \cdot \nabla \boldsymbol{V}_d = \frac{C_d Re_d}{24K}(\boldsymbol{V}_a - \boldsymbol{V}_d) + \left(1 - \frac{\rho_a}{\rho_w}\right)\frac{1}{Fr^2}\boldsymbol{g}, \tag{3-8}$$

where α is the water volume fraction, $\boldsymbol{V}_d$ the droplet velocity and ρ_w the density of water, C_d the drag coefficient of the droplet, K the inertial parameter and Fr the Froude number.

Collection efficiency can be obtained by

$$\beta = -\alpha \boldsymbol{V}_d \cdot \boldsymbol{n}, \tag{3-9}$$

where $\boldsymbol{n}$ is unit vector normal to the surface.

The velocity and liquid water content are then used to compute the flux of impinging water on a surface as

$$\dot{m}''_{imp} = LWC(V_\infty \beta). \tag{3-10}$$

The ICE3D module then uses results from the FENSAP (shear stress and heat transfer at surfaces) and DROP3D (water flux) modules to calculate ice accretion. The Messinger model [28] is implemented by representing the impinging droplets by a thin liquid film allowing for water runback caused by shear, centrifugal or gravitational forces. On solid surfaces, a system of two partial differential equations of mass and energy conservation is solved:

$$\rho_w\left(\frac{\partial h_f}{\partial t}+\nabla\cdot\left(\overline{\boldsymbol{V}}_{\boldsymbol{f}} h_f\right)\right)=\dot{m}_{imp}''-\dot{m}_{evap/sub}''+\dot{m}_{ice}'' \tag{3-11}$$

$$\rho_w\left(\frac{\partial\left(h_f c_{p,w} T_s\right)}{\partial t}+\nabla\cdot\left(\overline{\boldsymbol{V}}_f h_f c_{p,w} T_s\right)\right)=\dot{m}_{imp}''\left(\frac{\|\boldsymbol{V}_d\|^2}{2}+c_{p,w}\left(T_{d,\infty}-T_s\right)\right) \tag{3-12}$$

$$-\frac{1}{2}\dot{m}_{evap/sub}''\left(L_{evap}+L_{sub}\right)+\dot{m}_{ice}''\left(L_{fus}-c_{p,ice}\left(T_m-T_s\right)\right)$$

$$+c_h\left(T_{rec}-T_s\right)+Q_{anti-icing}\ ,$$

where h_f is the height of the water film, $c_{p,w}$ and $c_{p,ice}$ are respectively the specific heat capacities of water and ice, $\overline{\boldsymbol{V}}_f$ is the velocity of the water film, T_s is the equilibrium to temperature at the air, water, ice and surface interface, $T_m, T_{d,\infty}, T_{rec}$ correspond respectively to the melting, far field droplet and recovery temperatures. The latent heats of evaporation, sublimation and fusion are represented by L_{evap}, L_{sub} and L_{fus}. c_h is the convective heat transfer coefficient. Anti-icing heat flux is represented by the term $Q_{anti-icing}$. The mass fluxes of ice evaporation/sublimation and ice accretion are given respectively by $\dot{m}_{evap/sub}''$ and $\dot{m}_{ice}''$.

It is not difficult to see that the sets of partial differential equations first introduced by the 3 modules of FENSAP-ICE are “Navier-Stokes-like”, and can be handled with ease by the same or similar types of solvers. In addition, while it is impossible for control volume methods (not to be confused with finite volume methods) to extend 2D solutions to 3D, it is very simple for a 3D CFD code to represent 2D situations.

The glaze icing model (instead of rime icing) is adopted for all results in this research. A mesh movement tool using an arbitrary Lagrangian Eulerian method is integrated as an optional post-processing tool [29]. It provides a displaced mesh geometry that takes into account the ice thickness for an eventual FENSAP flow computation to assess the aerodynamic impact of the icing.

In the solid domain, the C3D module models heat conduction by the Poisson conduction equation. The conjugate heat transfer module CHT3D combines the previous modules and interfaces the solid and fluid domains data at the surface walls. All the modules are called at every CHT iteration as temperature and heat flux distributions at the boundaries are exchanged. In anti-icing mode, overall convergence is sought by converging each module and monitored by the change in surface temperature between each CHT iteration. The total simulation time is controlled by the number of global CHT iterations, the C3D conduction and ICE3D accretion times per CHT iteration. Flow, icing and solid conduction solutions are obtained at the end of a CHT3D computation.

3.2.2 CFD simulations

Distinct meshes for the fluid and solid domains are required to solve the conjugate heat transfer problem. The solid domain mesh is generated by the user to include layers and boundary conditions representing different material zones. The heating zone is initially flagged with a predetermined boundary condition for the optimization framework to then automatically generate the different heaters.

Initial computations for flow, droplet impingement, ice accretion and solid domain conduction are performed by the user, alongside the creation of a CHT3D template run. The framework then generates and conducts the necessary CHT simulations with the varying heating power and/or zones depending on the chosen design variables and parameters. CHT3D interfaces the outer surface of the solid domain with the corresponding rotor walls of the fluid domain and calls the FENSAP-ICE modules sequentially and iteratively to solve the conjugate heat transfer problem. Simulations are run in anti-icing mode where at each global CHT iteration, the surface thermal properties are updated from the different modules. In hover, the fluid mesh is either a relative frame of reference or a stitching mesh. The former offers the advantage of being less computationally intensive than the latter by imposing a rotational velocity to the fluid and solving steady RANS. For CHT3D to obtain the convective heat transfer values at each iteration in the fluid domain, the user can choose whether to resolve the full RANS equations (most expensive), resolve energy only (less expensive), or keep flow (and therefore the heat transfer coefficient) unchanged (least expensive). Thus, the user can choose one of the three options for relative frame of reference computations by assessing the trade-off between needed accuracy and available computational time. In the results presented in this thesis, only energy is resolved for relative frame of reference computations, while a constant heat transfer coefficient is used for mesh stitching.

3.2.3 Mesh stitching

With the exception of hovering rotors, general rotorcraft flows cannot be solved with relative frame of reference computations as the rigid rotation of the rotor is not considered. As such, mesh stitching is used to address these cases. Stitching meshes consist of a rotational grid containing the rotor(s) embedded within a stationary mesh. A gap exists between the two domains that, at every timestep, is stitched, then unsteady flow is solved. The gap is subsequently unstitched, ending with the rotational domain being rigidly rotated by the angle corresponding to the timestep [25]. Thus, mesh stitching enables the computation of unsteady rotorcraft flows containing a rotor and fuselage, multiple rotors or forward flight regime.

However, icing occurs on the timescale of minutes while rotorcraft flow time-stepping is on the order of milliseconds. With significant computational resources only allowing for a few rotations, a fully unsteady or multi-shot CHT approach is thus infeasible. Therefore, a periodically "averaged" flow field is obtained by averaging all the solutions composing the last rotor rotation. This averaged solution is provided to CHT3D and kept unchanged throughout the anti-icing CHT iterations, maintaining the heat transfer coefficient constant. Averaged solutions for droplet and icing are also initially provided prior to a CHT computation.

3.2.4 Aerodynamics-based optimization

The output ice solution from CHT3D is sufficient only if icing variables are considered in the optimization problem (maximum instantaneous ice accretion, for example). For an optimization problem based on aerodynamic variables, a further icing step using the ICE3D module is performed to generate a displaced mesh that accounts for the ice growth geometry. This is followed by a flow simulation on the displaced mesh to obtain torque and lift values. The additional stage of opting for direct aerodynamic variables approximately doubles the computational time. The user can therefore adjust whether it is desirable to obtain direct aerodynamic performance indicators at the expense of computational cost. However, the time increase occurs up-front during the initial generation of snapshots and has no influence on the time of the subsequent optimization iterations.

3.3 ROM-based optimization

3.3.1 ROM methodology

Solving optimization problems typically requires hundreds of function evaluations. Furthermore, computationally intensive CFD computations such as solving a rotor CHT problem, can necessitate hours or days to complete. As such, evaluating each optimizer-provided set of design variables by the CFD solver would make the problem intractable. Therefore, a metamodel built by ROM provides instantaneous objective and constraint function evaluations to the optimizer. The McGill CFD Lab's ROM tool is utilized in the optimization interface to significantly reduce computational time.

3.3.2 Design of Experiments

A DoE aims at sampling effectively and efficiently a design space. In this case, a set of finite snapshots is evaluated to obtain enough information for ROM to relate design variables to output function values from CFD. Thus, sampling of the design space is conducted first with the user choosing the number of snapshots N_S, the design space limits, as well as the sampling method. A uniform distribution following an LPτ method [30] is adopted as the design space characteristics (CFD function value distribution) are unknown initially [31]. LPτ is a sampling method introduced by Sobol, yielding a uniformly distributed sequence of numbers. The sequence is computed using lookup tables provided by Sobol and Statnikov [32]. Moreover, this deterministic sampling allows the addition of more snapshots while maintaining the uniformity of the sampling, a beneficial feature implemented in an error improvement strategy (Section 3.4.1). However, this method cannot be used to generate biased samples, where some areas of the design space are sampled more densely than others, a needed feature for another error improvement technique (see Section 3.4.5). Therefore, centroidal Voronoi tessellation (CVT), capable of performing uniform or biased sampling, is utilized with a density function when biased sampling is required [33]. Given an open set $\Omega \subseteq \mathbb{R}^{N_D}$ and a set of distinct points $\boldsymbol{z_i} \in \Omega, i = 1, \dots, s$, the Voronoi region $\hat{V}_i$ corresponding to the point $\boldsymbol{z_i}$ is defined as

$$\hat{V}_i = \{\boldsymbol{x} \in \Omega \mid \|\boldsymbol{x} - \boldsymbol{z_i}\| < \|\boldsymbol{x} - \boldsymbol{z_j}\| \; for \; j = 1, \dots, s, j \neq i\}, \tag{3-13}$$

where $\|\cdot\|$ denotes the Euclidean norm in $\mathbb{R}^{N_D}$, the points $\{\boldsymbol{z_i}\}_{i=1}^{s}$ are named generators of the Voronoi regions and the set $\{\hat{V}_i\}_{i=1}^{s}$ is a Voronoi tessellation of Ω. Given a density function $\rho(\boldsymbol{x})$ defined in $\hat{V}_i$, the mass centroid $\boldsymbol{z_i^*}$ of the Voronoi region $\hat{V}_i$ is

$$\boldsymbol{z_i^*} = \frac{\int_{V_i} \boldsymbol{x} \rho(\boldsymbol{x}) d\boldsymbol{x}}{\int_{V_i} \rho(\boldsymbol{x}) d\boldsymbol{x}}. \tag{3-14}$$

The Voronoi tessellation is called a centroidal Voronoi tessellation if and only if the generators are also the mass centroids of the Voronoi, namely

$$\boldsymbol{z_i} = \boldsymbol{z_i^*}, i = 1, \dots, s. \tag{3-15}$$

In the context of discrete CVT, the set Ω is represented by a set of discrete points W=$\{\boldsymbol{x}_i\}_{i=1}^{N_S} \in \mathbb{R}^{N_D}$. The Voronoi regions corresponding to generators $\{\boldsymbol{z_i}\}_{i=1}^{s} \in \mathbb{R}^{N_D}$ are defined as

$$\hat{V}_i = \{\boldsymbol{x} \in W \mid \|\boldsymbol{x} - \boldsymbol{z_i}\| \leq \|\boldsymbol{x} - \boldsymbol{z_j}\| \; for \; j = 1, \dots, s, j \neq i, \tag{3-16}$$

where the equality holds only for $i < j$ and the mass centroid $\boldsymbol{z}^*$ of a Voronoi region $V \subset W$ is given by

$$\sum_{\boldsymbol{x} \in V} \rho(\boldsymbol{x}) \, \|\boldsymbol{x} - \boldsymbol{z}^*\|^2 = \inf_{\boldsymbol{x} \in V^*} \sum_{\boldsymbol{x} \in V} \rho(\boldsymbol{x}) \, \|\boldsymbol{x} - \boldsymbol{z}\|^2, \tag{3-17}$$

where V^* can be taken to be V or a larger set such as $\mathbb{R}^{N_D}$. Discrete CVT is implemented by Lloyd's method, using a two-step iterative process between constructing Voronoi tessellation and replacing generators with the mass centroids [34]. Uniform sampling is performed by setting the density function to $\rho(\boldsymbol{x}) = 1$. In Section 3.4.5 the biasing is provided by a density function defined by the error distribution obtained from the leave-one-out cross-validation procedure explained in Section 3.4.1.

3.3.3 Proper orthogonal decomposition

The optimization framework automatically translates the list of samples into all the necessary FENSAP-ICE runs with the changed individual heater powers and heating zones. Once high-fidelity snapshot generation is concluded, the framework postprocesses raw results, extracting and formatting the relevant icing or aerodynamic output data for the user defined optimization problem statement. The ROM tool supports metamodels based on FENSAP solution files. However, scalar objective function (or constraint) icing or aerodynamic quantities from the solutions are used to build the metamodel instead of the entire vector solution representing the flow field. This has the benefit of reducing the cost of the ROM (interpolating for a scalar instead of a vector with potentially millions of entries) and thus accelerating the optimization process [35]. The optimization framework then builds the metamodel using proper orthogonal decomposition and Kriging to perform solution interpolation, instantly responding to constraints and objective function queries by the optimizer.

Spectral methods are numerical methods that seek to express differential equations as a sum of basis functions. POD is a physics-based spectral method used to extract basis functions from a set of snapshots. The implementation of POD used by the McGill CFD Lab ROM tool utilizes the cost-effective "method of snapshots" proposed by Sirovich [36].

The DoE yields N_S snapshots $\{\boldsymbol{U_1}, \dots, \boldsymbol{U_{N_S}}\}$, where $\boldsymbol{U_i} = \boldsymbol{U}(\boldsymbol{x_i}) \in \mathbb{R}^{N_P}$, and $\boldsymbol{x_i} \in \mathbb{R}^{N_D}$. For the sake of generality, the snapshot $\boldsymbol{U}$ is represented by a vector. For standard optimization runs in this research, it is instead a scalar containing the value of the objective function of interest. However, it is a vector (of dimension N_P) if the user opts for a snapshot representing the entire flow field or the ice solution, as outlined in upcoming error improvement (Section 3.4.3). The vector $\boldsymbol{x}$ contains the N_D design variables of the problem. An interpolated solution $\boldsymbol{U}(\boldsymbol{x_\delta})$ in the design space, at an untried location $\boldsymbol{x_\delta}$, can be approximated by a linear combination of basis functions and coefficients

$$\boldsymbol{U}(\boldsymbol{x_\delta}) = \sum_{j=1}^{m<N_S} \omega_j^\delta \, \boldsymbol{\varphi}_\mathrm{j} \ , \tag{3-18}$$

where m represents the number of dominant modes retained based on the desired energy content and $\boldsymbol{\varphi}_\mathrm{j}$ is a modal basis function. In fluid dynamics, specifying a-priori an appropriate modal basis function type is impossible (unlike, for example, in the field of vibration where

Fourier series are appropriate) [35]. Therefore, POD constructs basis functions as a linear combination of the snapshot and a weight coefficient. An optimization problem is solved to minimize the error over the domain and select optimized linear basis functions. As such, set of m functions are used to span the design space and are expressed by

$$\boldsymbol{\varphi}_{\mathrm{j}} = \sum_{i=1}^{N_S} \zeta_i^j \, \mathbf{U}_{\mathrm{i}}, \tag{3-19}$$

where ζ is a weight coefficient obtained by solving for the eigenvector $\boldsymbol{\zeta}$ of the correlation matrix $\boldsymbol{R}$ of size $N_S \times N_S$ such that

$$\boldsymbol{R\zeta} = \boldsymbol{\Lambda\zeta}\,, \tag{3-20}$$

where

$$\boldsymbol{R} = \frac{1}{N_S} \boldsymbol{A^T A} \tag{3-21}$$

and

$$\boldsymbol{A} = \{\boldsymbol{U_1}, \dots, \boldsymbol{U_{N_S}}\}, \tag{3-22}$$

where ω_j^δ is a coefficient obtained from a Kriging interpolation of a response surface (which is metamodel, not to be confused with the overall POD metamodel). As such, each mode $\boldsymbol{\varphi}_{\mathrm{j}}$ has a corresponding response surface mapping an input $\boldsymbol{x}_i$ to an output ω_j^i . This surface is formed by the projection coefficients ω_j^i , $i = 1, \dots, N_S$ expressed as

$$\omega_j^i = \boldsymbol{U_i} \,.\, \boldsymbol{\varphi}_{\mathrm{j}}\,. \tag{3-23}$$

The Kriging interpolation requires solving an internal optimization problem for the maximization of the likelihood function. This process is explained in the next section.

3.3.4 Kriging

Kriging is a method developed in geostatistics by a mining engineer named Krige in 1951. Initially geared towards the exploration of mining deposits, the method is today used to build response surfaces for numerous applications such as engineering design and optimization. The interpolation function is a realization from a Gaussian stochastic process [37]. A function value $\hat{y}(\boldsymbol{x_\delta})$ (in this case ω_j^i) at an untried location x_δ is found by the Kriging predictor

$$\hat{y}(\boldsymbol{x_\delta}) = \hat{\mu} + \boldsymbol{r}'\boldsymbol{R}^{-1}(\boldsymbol{y} - 1\hat{\mu}), \tag{3-24}$$

where y is the vector of the observed function values, given by

$$\boldsymbol{y} = \begin{pmatrix} y_1 \\ \vdots \\ y_{N_S} \end{pmatrix}. \tag{3-25}$$

The remaining variables stem from error analysis. The error at a sampled point is zero as the interpolation function passes exactly through them. At an unevaluated point (located between sampled points), the error measures the uncertainty of the predictor. The uncertainty is modeled by a random variable $Y(\boldsymbol{x})$ which follows a normal distribution of mean μ and covariance σ^2. Assuming a continuous and smooth function and considering two points $\boldsymbol{x_i}$ and $\boldsymbol{x_j}$, the correlation between the two random variables $Y(\boldsymbol{x_i})$ and $Y(\boldsymbol{x_j})$ is given by

$$Corr\left[Y(\boldsymbol{x_i}), Y(\boldsymbol{x_j})\right] = \exp\left(\sum_{l=1}^{N_D} \theta_l \left|x_{il} - x_{jl}\right|^2\right). \tag{3-26}$$

The correlation matrix $\boldsymbol{R}$ is a symmetric $N_S \times N_S$ matrix with R_{ij} given by equation (3-26), and the vector $\boldsymbol{r}$ is given by

$$\boldsymbol{r} = \begin{pmatrix} Corr\left[Y(\boldsymbol{x}^{\boldsymbol{\delta}}), Y(\boldsymbol{x}_{\boldsymbol{i}})\right] \\ \vdots \\ Corr\left[Y(\boldsymbol{x}^{\boldsymbol{\delta}}), Y(\boldsymbol{x}_{\boldsymbol{N_S}})\right] \end{pmatrix}. \tag{3-27}$$

The correlation parameter $\theta_l(> 0)$ is sought by maximizing the concentrated log-likelihood function [37]

$$Li(\boldsymbol{\theta}) = -\frac{N_S}{2}\log(\hat{\sigma}^2) - \frac{1}{2}\log(|\boldsymbol{R}|), \tag{3-28}$$

where

$$\hat{\mu} = \frac{\boldsymbol{1}'\boldsymbol{R}^{-1}\boldsymbol{y}}{\boldsymbol{1}'\boldsymbol{R}^{-1}\boldsymbol{1}} \tag{3-29}$$

and

$$\hat{\sigma}^2 = \frac{(\boldsymbol{y} - \boldsymbol{1}\hat{\mu})'\boldsymbol{R}^{-1}(\boldsymbol{y} - \boldsymbol{1}\hat{\mu})}{N_S}. \tag{3-30}$$

The maximization of the log-likelihood function is done by a hybrid approach combining a genetic algorithm and a gradient-based quasi-Newton line search method [33]. In this optimization problem, $\boldsymbol{\theta} \in \mathbb{R}^{N_D}$ is the vector of design variables and $f(\boldsymbol{\theta}) = -Li(\boldsymbol{\theta})$ the objective function to minimize. To solve this problem, Lappo [38] adopted a genetic algorithm as it is argued to be more robust at finding a global optimum (and avoiding a local optimum) than gradient-based methods for highly nonlinear objective functions. However, genetic algorithms are time-consuming compared to gradient-based algorithms. Therefore, Zhan [39] implemented and combined to the previous framework a BFGS (Broyden, Fletcher, Goldfarb and Shanno) line search method to accelerate the search for a global optimum.

3.3.5 Optimization algorithm

The optimization metamodel stems from sampling a high-fidelity CFD model in which the complex, highly nonlinear relationship between design variables and the objective function is represented. Thus, the design space can potentially be discontinuous, noisy and without defined gradients. Therefore, derivative-free optimization must be used and gradient-based methods are not considered. Hence, the derivative-free optimization software package NOMAD is used in this framework as its Mesh Adaptive Direct Search algorithm implementation includes a poll step from which global convergence properties are obtained [40]. The large number of iterations needed by NOMAD is an inconsequential drawback within the context of this framework given the use of ROM.

NOMAD performs optimization by using a search and a poll step at each iteration. The search step is optional and can be performed using a range of methods including metamodels [41] and heuristics. In this work, NOMAD's default search step option employing a quadratic model search is used [42]. The search step is performed first by creating a model within the current poll size and evaluating trial points expected to minimize the model. If a better point is found, then the current solution is updated, and the next iteration is started. Otherwise, the poll step is initiated.

The discrete mesh is defined at each iteration k by the following set

$$\boldsymbol{M_k} = \{\boldsymbol{x} + \Delta_k^m \boldsymbol{D}\boldsymbol{z} : \boldsymbol{z} \in \mathbb{N}^{n_D}, \boldsymbol{x} \in \boldsymbol{X_k}\} \subset \mathbb{R}^{N_D}, \tag{3-31}$$

where $\boldsymbol{X}_k = \{\boldsymbol{x_1}, \boldsymbol{x_2}, \dots\}$ is the set of all points previously evaluated by the start of iteration k.

At every iteration, the poll step generates a set of trial points by:

$$\boldsymbol{P_k} = \{\boldsymbol{x_k} + \Delta_k^p \boldsymbol{d} : \boldsymbol{d} \in \boldsymbol{D_k} \subset \boldsymbol{D}\} \subset \boldsymbol{M_k}, \tag{3-32}$$

where $\boldsymbol{x_k}$ is the current solution at iteration k, $\boldsymbol{x_k} \in \mathbb{R}^{N_D}$, Δ_k^p is the poll size parameter, Δ_k^m is the mesh size parameter and n_D is the number of directions. $\boldsymbol{D}$ is a positive spanning set of n_D directions whose non-negative linear combinations span $\mathbb{R}^{N_D}$. $\boldsymbol{D_k}$ is a positive spanning set of poll directions that are an integer combination of directions of $\boldsymbol{D}$.

The generated points are evaluated and, if a better solution is not found, the mesh is refined by decreasing the values of the poll and mesh size parameters. The process of poll step, evaluation and refinement for successive iterations failing to improve the solution is shown in Figure 2 for a 2D mesh. The algorithm terminates when the maximum number of iterations set by the user is reached or the minimum supported mesh size is attained. As the number of iterations increases, the MADS algorithm globally converges (independently of the starting point) toward an optimum that satisfies local optimality conditions based on Clarke's calculus for non-smooth functions [43].

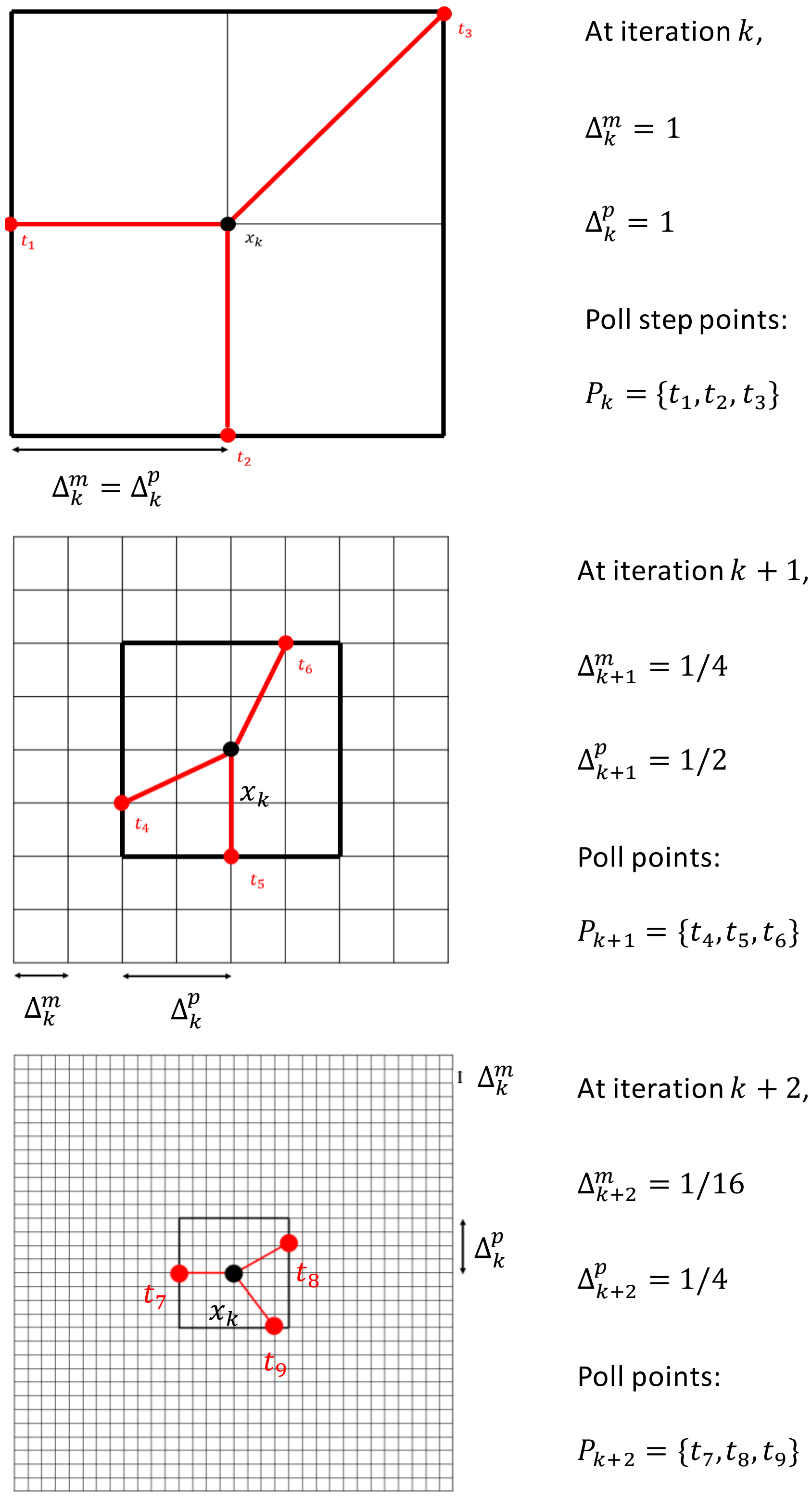

Figure 2: Mesh refinement and poll step point generation for three consecutive iterations, adapted from [19]

3.4 ROM error improvement

3.4.1 Leave-one-out cross-validation

While offering the advantage of making the problem less computationally intensive, the ROM-based objective and constraint function evaluations in the optimization process are not the direct results of CFD simulations. Therefore, it must be verified that the local accuracy of the ROM is adequate to ensure that generated results are meaningful. As such, leave-one-out cross-validation (LOOCV) is conducted to gauge the error at any point in the domain. To perform LOOCV, the objective function value is evaluated at every snapshot point using a model built on all other snapshots except the one at the current point.

In other words, for N_S snapshots $\{\boldsymbol{U_1}, \dots, \boldsymbol{U_{N_S}}\}$, where $\boldsymbol{U_i} = \boldsymbol{U}(\boldsymbol{x_i}) \in \mathbb{R}^{N_P}$, and $\boldsymbol{x_i} \in \mathbb{R}^{N_D}$, a solution is evaluated at a snapshot location $\boldsymbol{x_i}$ by using a metamodel built using $N_S - 1$ snapshots excluding $\boldsymbol{U_i}$.

This operation is repeated N_S times to obtain solutions at all DoE points. These are compared to their respective snapshots and a relative error measurement is obtained. Thus, this operation yields a vector of length N_S containing the LOOCV error at every datapoint. This data can be aggregated by taking an average of all the entries to obtain a measure of the error in the domain as well as for comparing different error improvement strategies. Furthermore, the maximum error in the LOOCV vector can also be retained as a performance gauge for the model. Four error improvement strategies based on LOOCV are proposed and implemented in the results section.

3.4.2 Uniform addition of snapshots

The addition of snapshots following uniform sampling to enrich a model is a simple starting point. With the sampling method being LPτ, the addition of snapshots does not disturb the uniformity of the DoE points. However, this method is computationally expensive as each additional snapshot can take hours to generate for an a-priori unknown marginal improvement in the LOOCV error.

3.4.3 Localization

Localization is a strategy utilized to negate the influence of snapshots located "far" in the design space from the iteration point [35]. As such, at every iteration, a new ROM is created with only the closest pre-defined number of snapshots to the evaluation point. This strategy of design space restriction during the optimization process comes with no time increase to the optimization process as the creation of a metamodel based on scalar objective function values is instantaneous.

3.4.4 CFD vector snapshots

Currently, a snapshot is a scalar quantity derived from a CFD solution vector with millions of entries describing an entire flow field or ice solution. This strategy aims to conserve more information about the original physics of the problem by employing solution vectors as snapshots instead. Therefore, the usage of CFD solutions as snapshots instead of the scalar values of icing or aerodynamic variables can be predicted to yield a more accurate metamodel without the need of additional snapshots. Furthermore, the ROM tool was designed for this specific use case, recreating complete CFD and icing solutions using ROM [33, 44]. However, this comes at the cost of an increased interpolation time, a critical operation that is performed at every iteration of an optimization run.

3.4.5 Error-driven sampling

The addition of snapshots to enrich the metamodel can be improved by focusing on regions of high error. Error-driven sampling allows for the efficient utilization of additional high-fidelity simulations by improving the areas of high error in the design space and thus reducing the LOOCV error. The ROM tool provides a LOOCV module with error-driven sampling. This capability is further developed to interface with the IPS optimization framework to efficiently generate new sampling points, augmenting the DoE to reduce the maximum LOOCV error in the domain. In this case, the tool first defines a density function for each dimension (design variable) in the design space based on the error distribution over the domain. The user controls the error threshold for adding samples and the total number of additional samples desired [44]. CVT sampling is then conducted to obtain new points to evaluate, biased by the error distribution from the previous DoE.

3.5 Summary of the proposed framework

Figure 3 summarizes the methodology described previously.

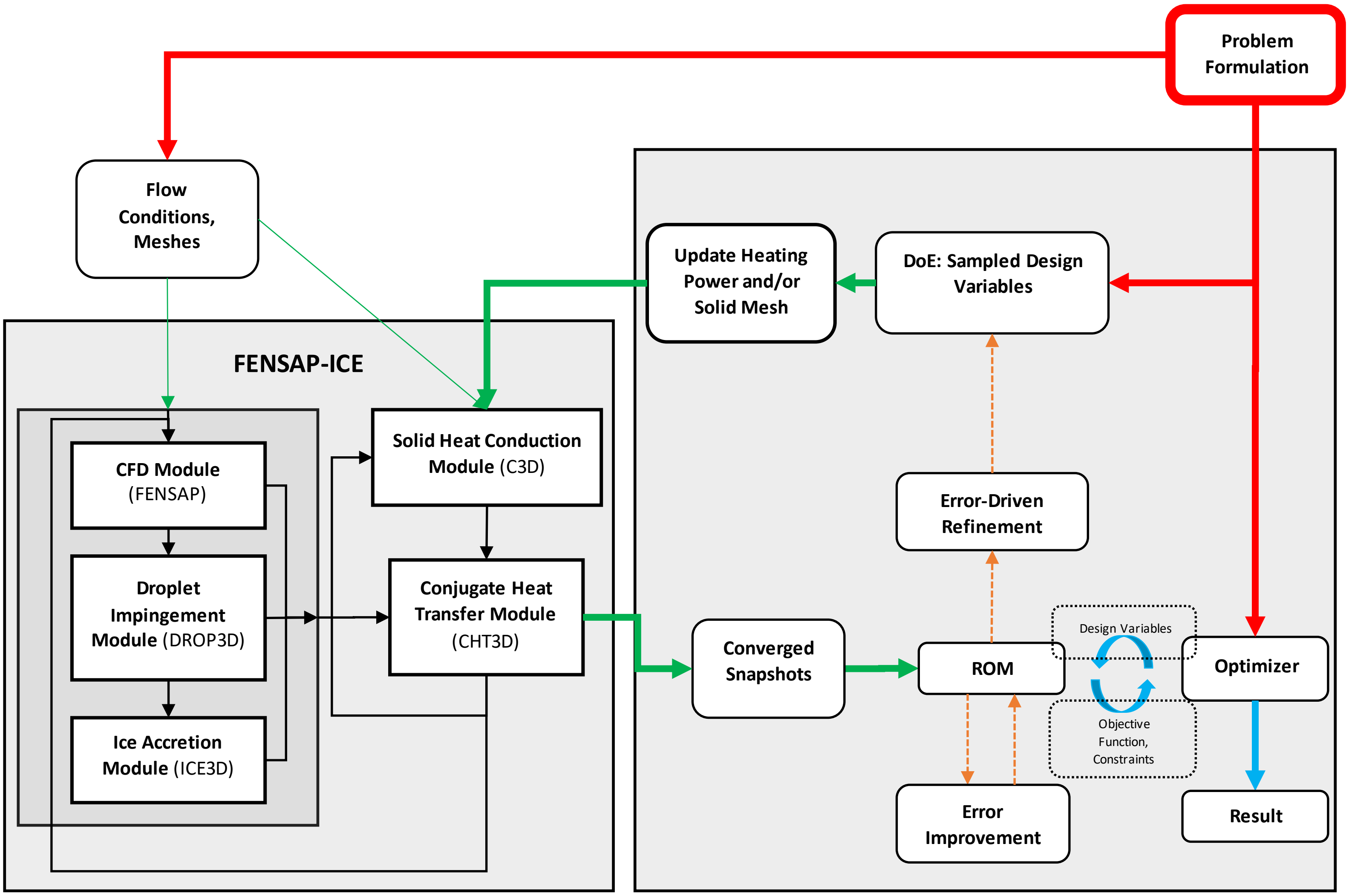

Figure 3: Methodology summary flowchart

4 Numerical results

4.1 Rationale

The optimization results of four problem formulations are shown in this section. Cases 1, 2 and 3 follow a common geometry based on the Caradonna-Tung experiments [45] with common properties outlined in Table 1. Case 4 uses mesh stitching and its setup is listed in Table 9. The chordwise distribution of heaters is based on the concept of the Sikorsky ETRIPS [10]. Case 1 minimizes the maximum ice accretion rate with respect to heating power while obeying a maximum power constraint. As neither the objective nor constraint functions necessitate solving the flow around the iced mesh during the snapshot generation, it is the least computationally costly case to study all four. However, when constraint relaxation analysis is conducted, it is found that while the objective function value is reduced, the overall aerodynamic impact worsens. Therefore, subsequent cases use torque-related objective or constraint functions instead, increasing the computational cost to solve a more suitable problem formulation. As such, Case 2 is a power minimization problem with respect to heating power subject to a maximum allowable torque rise. While Case 2 shows the versatility of the tool by its ability to change objective and constraint functions, Case 3 expands the number of design variables by introducing the extent of the heating zone. Thus, in Case 3, torque is minimized with respect to both heating power and heating zone extent, while following a maximum heating power constraint. Finally, the first three cases use a relative frame of reference method which is limited to hovering rotors. Thus, Case 4 serves to demonstrate the use of a stitching mesh, a powerful method that enables more complex rotorcraft configurations.

Rotor	Caradonna-Tung
Airfoil	NACA 0012
Rotor radius	1.143 m
Chord	0.1905 m
Collective pitch	8°
Twist	0°
Mesh sizes: fluid / solid	14 765 571 / 1 090 680
Flight regime / mesh type	Hover / Relative frame of reference
RPM	650
Heaters	5

Table 1: Common properties for Cases 1,2,3

Material	**Density (kg/m^3)**	**Thermal conductivity (W/m/K)**	**Enthalpy at 0°C (J/kg)**	**Thickness (mm)**
Titanium	4540	17.03	141310.5	1
Fiberglass	1794	0.294	428859.16	1

Table 2: Solid mesh material properties for Cases 1,2,3

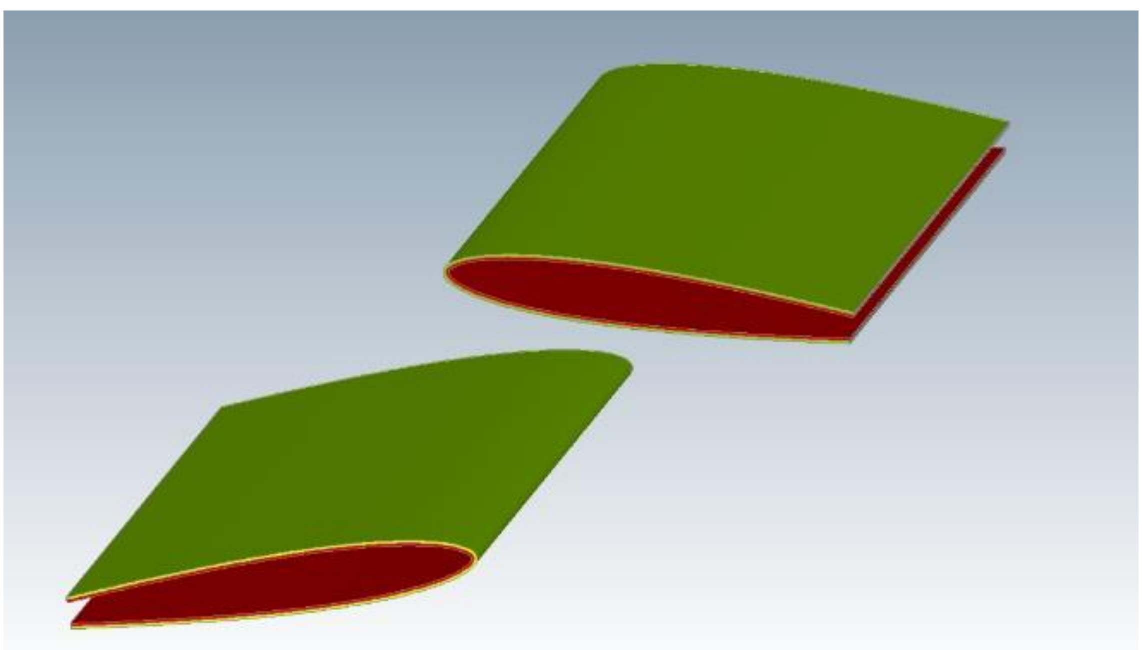

Figure 4: Material layers illustration for Cases 1,2,3

For all four cases, the heater layout is chordwise with two material zones in the solid domain, titanium and fiberglass, shown respectively in green and red in Figure 4. The heating zone protects the entire rotor along the span and 25% of the chord in the solid domain for cases 1 and 2 while its extent is variable in Case 3. As shown in Figure 5, heater 1 (red) implements a "parting strip" design on the leading edge, heaters 2 (green) and 3 (blue) follow behind, respectively, in the chordwise direction on the upper surface and similarly to 4 (orange) and 5 (lime) on the lower surface.

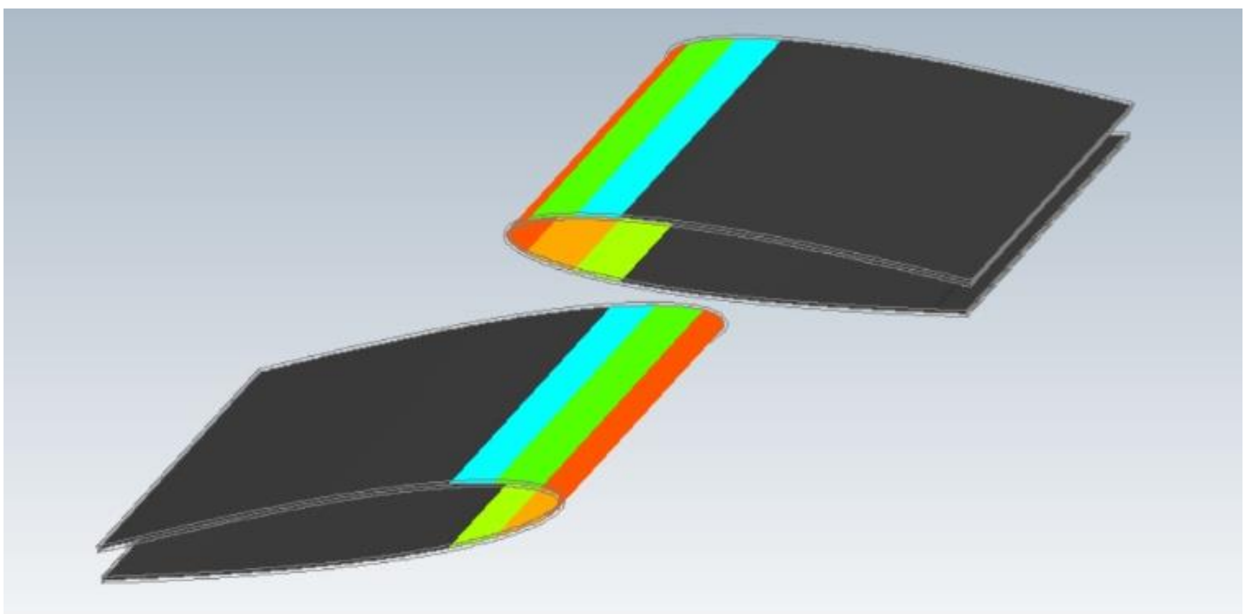

Figure 5: Heater layout for Cases 1 & 2 located in the two material layers

4.2 Case 1: ice accretion minimization

In the first case, the minimization of the instantaneous ice accretion rate is sought while respecting a maximum heating power constraint.

4.2.1 Problem formulation

Number of snapshots	50
Snapshot icing time (s)	10
OAT (K)	260
LWC (g/m^3)	1
MVD (µm)	20
Objective function	Maximum instantaneous ice accretion rate
Constraint	Total Electric Power: 100, 200, 300 & 400 Watts

Table 3: Case 1 properties

4.2.2 Optimization results and constraint relaxation analysis

This case presents a situation of optimization under lack of power where the IPS is unable to yield an ice-free surface. As such, the minimization of ice accretion variables may not necessarily lead to a minimization of adverse aerodynamic effects. The optimized results for 100, 200, 300 and 400 watts are iced for an additional 300 seconds followed by mesh displacement and flow computations. Table 4 shows that while constraint relaxation leads to improvements in the optimized objective function results, when mesh displacement and flow computations are performed, the aerodynamic impact worsens. As such a 7.2% reduction in the objective function leads to a 14% increase in torque. In this case, it is found that the available power is insufficient to reduce runback ice refreezing further down the chord. Therefore, the optimization framework will utilize torque as an objective function (or constraint) in subsequent problem formulations.

Heating power constraint (W)	Optimized maximum instantaneous Ice growth (10^{-2} kg/m^2/s)	CFD solution lift (N)	CFD solution torque (N.m)
100	3.013	75.09	16.98
200	2.926	73.78	18.09
300	2.805	72.97	18.37
400	2.796	71.05	19.37

Table 4: Case 1 results

4.3 Case 2: power optimization

A new DoE is performed based on values of torque following the conditions given in Table 5. Aerodynamic values for clean and unprotected cases are obtained (Table 6). Figures 6 and 7, respectively, show the ice accretion on an unprotected rotor and the corresponding displaced mesh. Total electric power is minimized with respect to a maximum allowable torque rise of 1% as compared to a clean rotor configuration. Starting from an initial uniform heater power density, a reduction in power consumption of 59% is achieved while respecting the imposed constraint on allowable torque rise. The lowest reduction in power density is observed in the aftmost heaters which is consistent with an attempt at limiting the buildup of refreezing runback ice.

Number of Snapshots	50
Snapshot Icing Time (s)	300
OAT (K)	260
LWC (g/m^3)	1
MVD (µm)	20
Objective Function	Total Electric Power
Constraint	Torque rise: 1%

Table 5: Case 2 properties

Configuration	Lift (N)	Torque (N.m)
Clean	78.58	14.99
Unprotected	70.92	21.02

Table 6: Clean and unprotected rotor lift and torque results

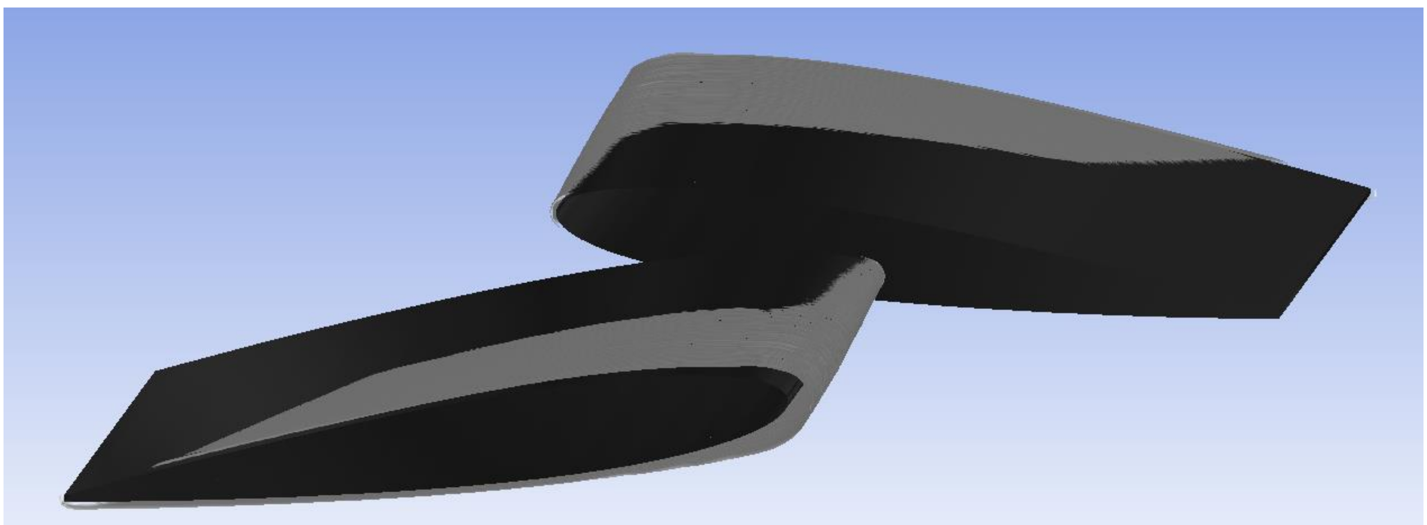

Figure 6: Ice growth on unprotected rotor

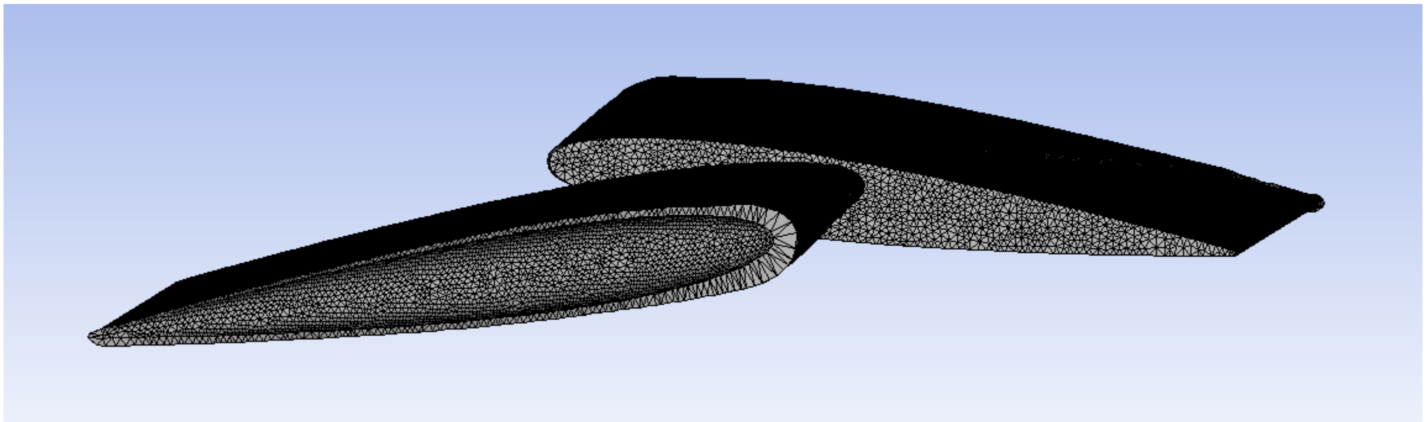

Figure 7: Iced rotor grid with mesh displacement

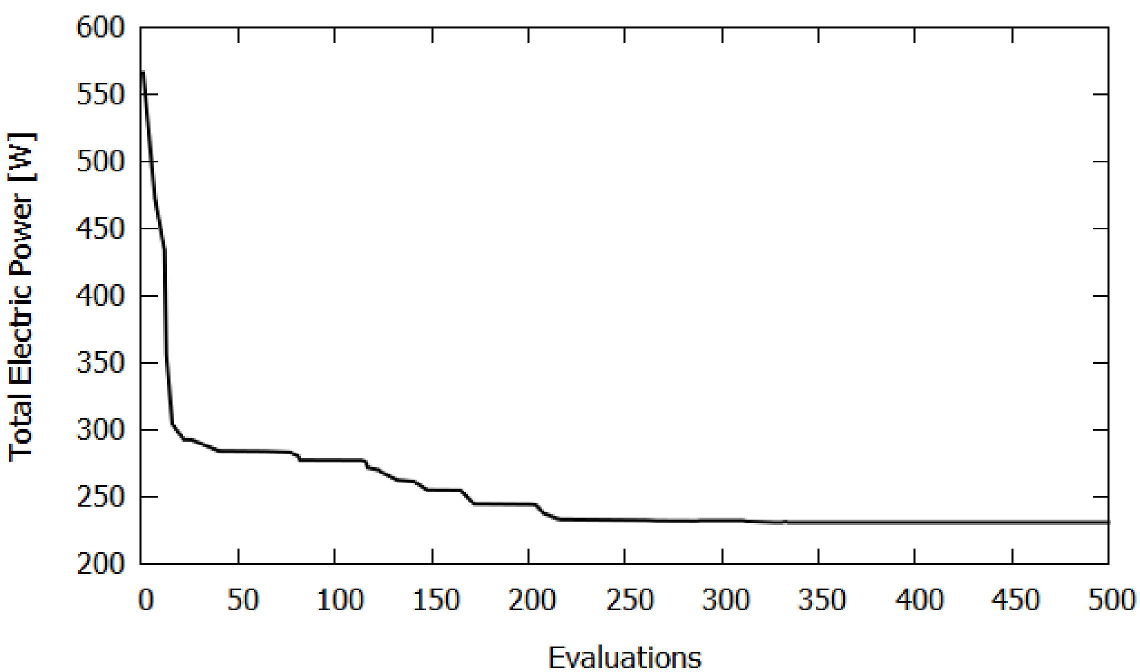

Figure 8: Case 2 final optimization run

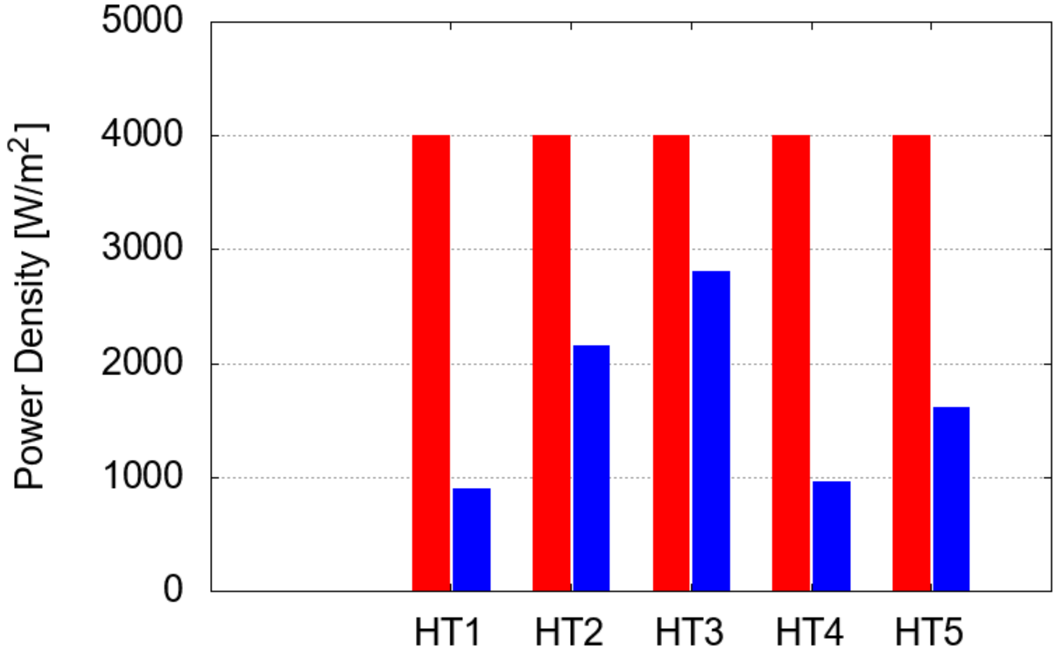

Figure 9: Case 2 initial (red) and optimized (blue) heating power

4.4 Case 3: extent & power optimization

In addition to the five heaters' power densities, this problem formulation adds four design variables to describe the extent of the protected zone. (1) the percentage of protected chordwise surface of the upper surface, (2) that of the lower surface, (3) the unprotected spanwise surface starting from the root and (4) that starting from the tip. The heaters' distribution pattern remains unchanged with a chordwise configuration and a leading edge parting strip. The five independent heating zones are shown by the different colours in Figures 12 and 13.

Number of Snapshots	90
Snapshot Icing Time (s)	300
OAT (K)	260
LWC (g/m^3)	3
MVD (µm)	25
Objective Function	Torque
Constraint	Total Electric Power: 250 Watts

Table 7: Case 3 properties

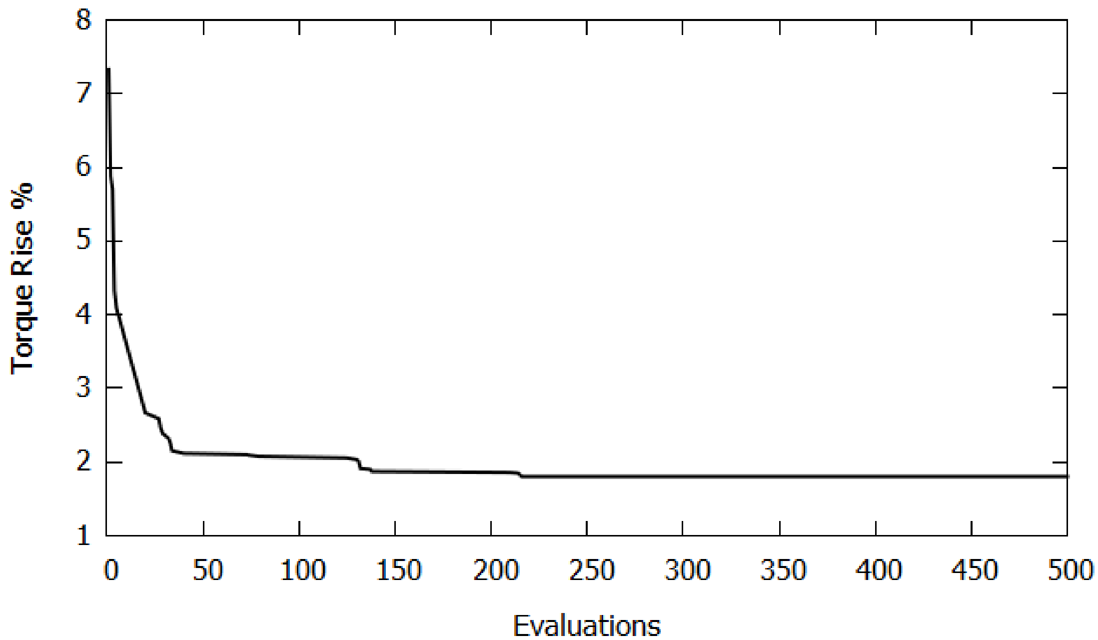

Figure 10: Case 3 final optimization run

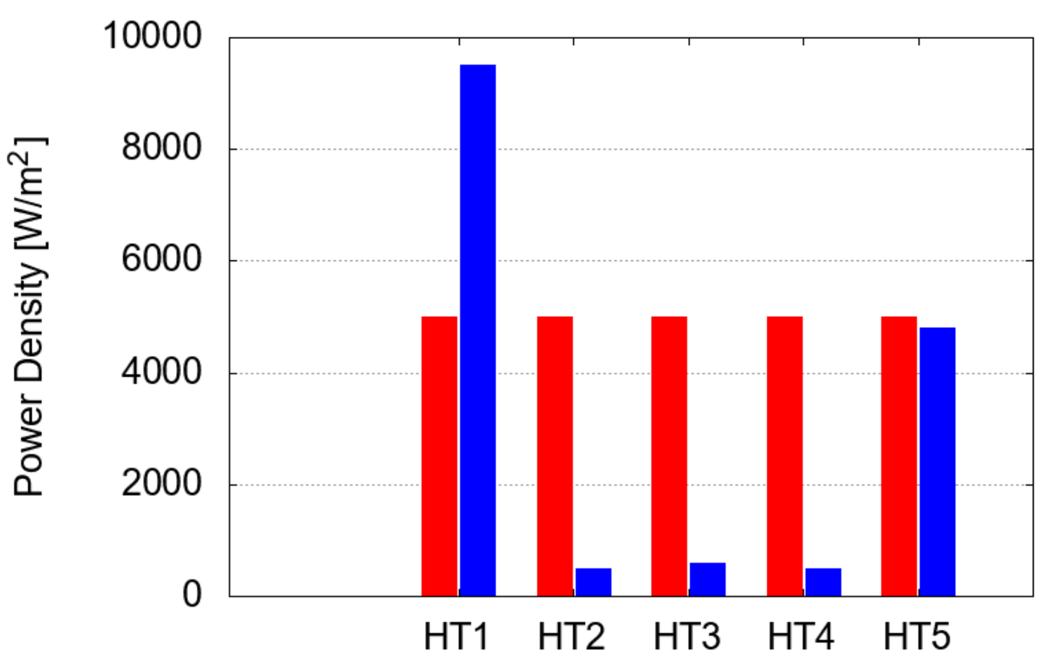

Figure 11: Case 3 initial (red) and optimized (blue) heating power

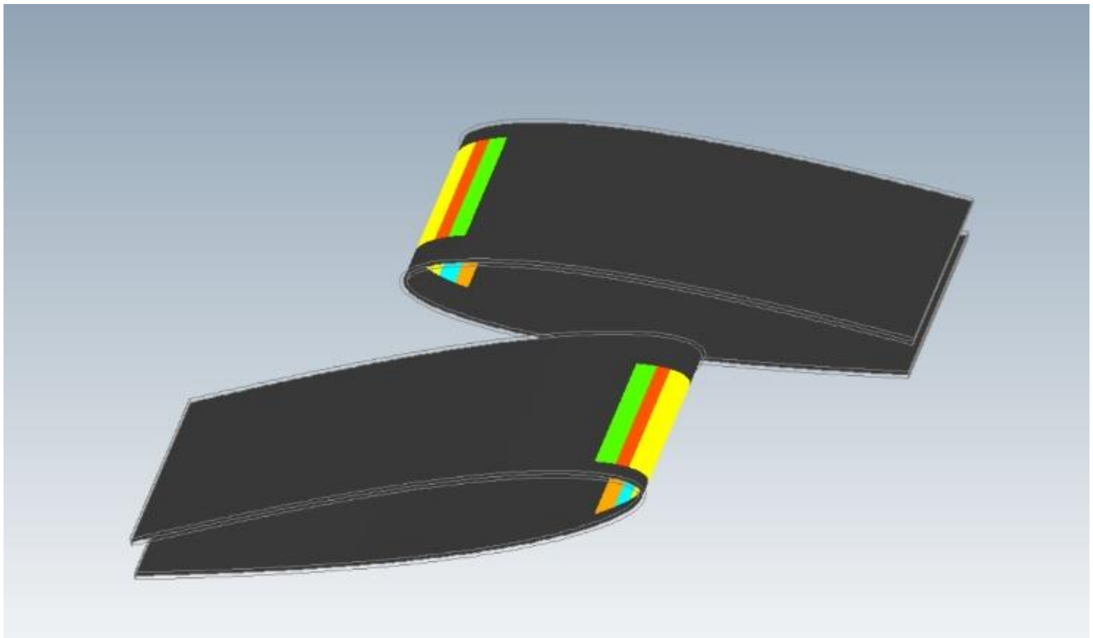

Figure 12: Case 3 initial heating zone extent

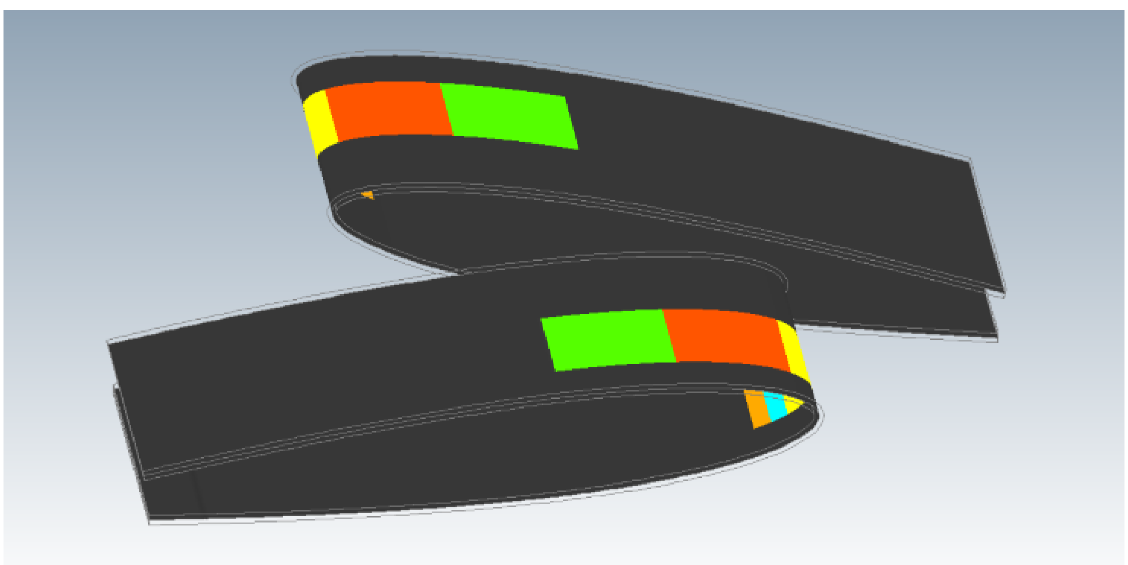

Figure 13: Case 3 final heating zone extent

The nine-variable optimization problem is initialized using uniform heating densities of 5000 W/m^2, a chordwise protected extent of 10% on both the upper and lower surfaces, an unprotected spanwise extent of 20% from the root and 10% from the tip. With a total power constraint of 250 W, the optimized configuration leads to a 7.3% to 1.8% reduction in iced rotor's torque rise. The optimizer achieves this result by maximizing the leading edge heating density and increasing the extent of the protected zone on the upper surface (42.7%). However, this comes at the cost of a reduction in the spanwise protection from the root (40%), the tip (20%) together with a substantial decrease in the heating power of the upper heating zones and of the first lower heating zone (in blue in Figure 13). The lower heating zone is somewhat reduced to protect only 8% of the lower surface and the aftmost lower surface zone heating power is slightly decreased to 4800 W/m^2.

4.5 Case 4: stitching mesh torque minimization

Case 4 geometry is based on the AERTS rotor [46]. The fluid domain utilizes a stitching mesh and a cross-section of the computational domain showing the unstitched gap can be seen in Figure 15. The solid domain heating zone is located two material layers below the surface. The three material layers used are an erosion shield, an elastomer and fiberglass as per Table 10. This optimization case seeks to minimize torque while respecting a maximum power constraint of 3000 W. Optimization of the heating power configuration decreases the percentage rise in required aerodynamic torque compared to a clean rotor (17.6 N.m) from 9.4% to 2.4%.

Rotor	AERTS
Airfoil	NACA 0015
Radius	1.17 m
Chord	0.173 m
Collective pitch	2.5°
Twist	-2.1°

Table 8: Case 4 geometry

Number of snapshots	50
Collective pitch (°)	2.5
Mesh sizes fluid / solid	11 616 702 / 1 017 660
Rotor diameter (m)	2.34
Flight regime / mesh type	Hover / stitching mesh
RPM	600
Snapshot icing time (s)	300
OAT (K)	263
LWC (g/m^3)	1.3
MVD (µm)	15
Number of materials	3
Heaters	5
Protected zone	Full span, 40% chordwise
Objective function	Torque
Constraint	Total Electric Power: 3000 Watts

Table 9: Case 4 properties

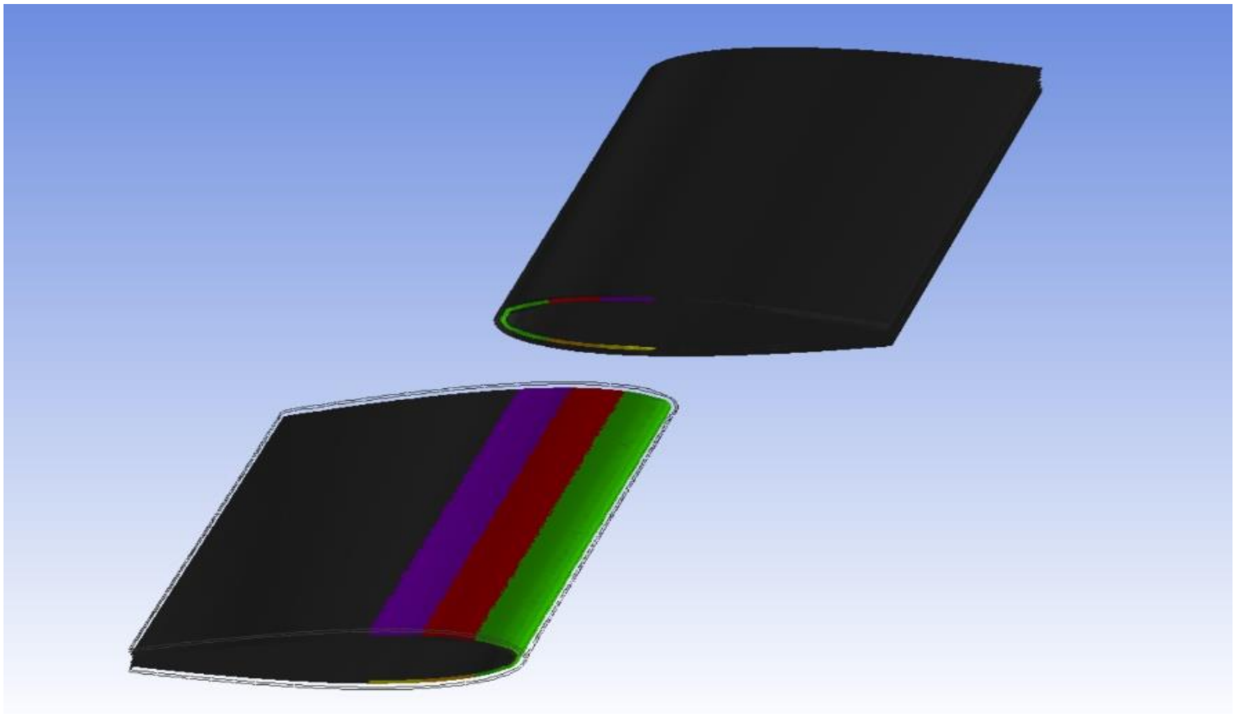

Figure 14: Heater layout for Case 4

Material	Density (kg/m^3)	Thermal conductivity (W/m/K)	Enthalpy at 0^{o}C (J/kg)	Thickness (mm)
Erosion shield	8025.25	16.26	137234.93	1
Fiberglass	2700	0.313	393160.4	1.5
Elastomer	1383	0.2561	343087.33	1.5

Table 10: Solid mesh material properties for Case 4

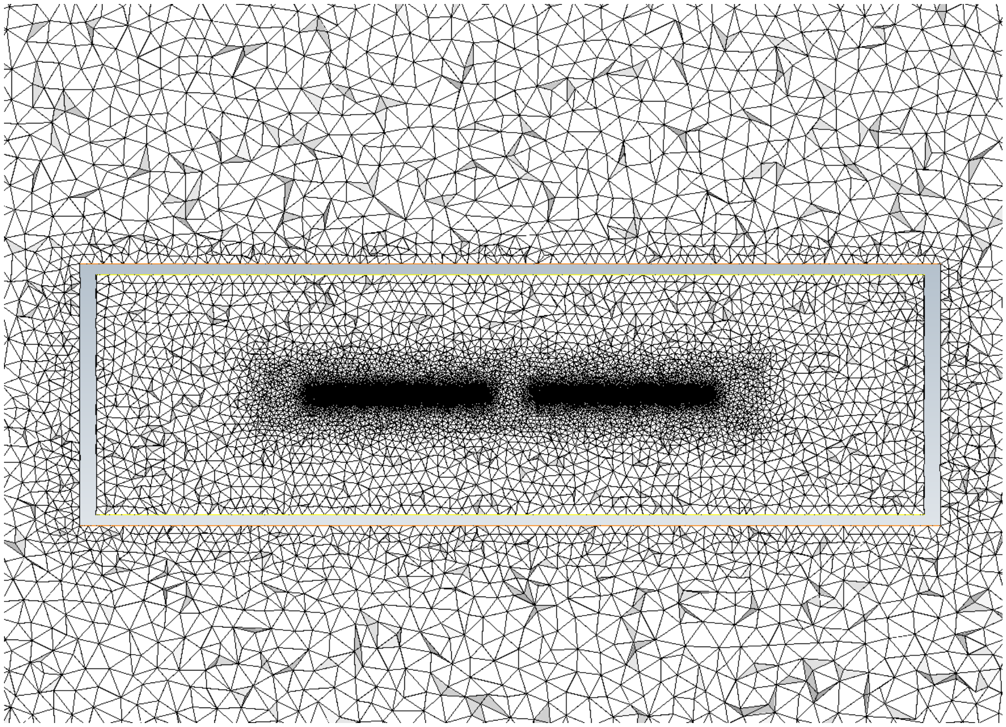

Figure 15: Case 4 fluid domain mesh cross-section with unstitched gap [47]

4.5.1 Optimization results

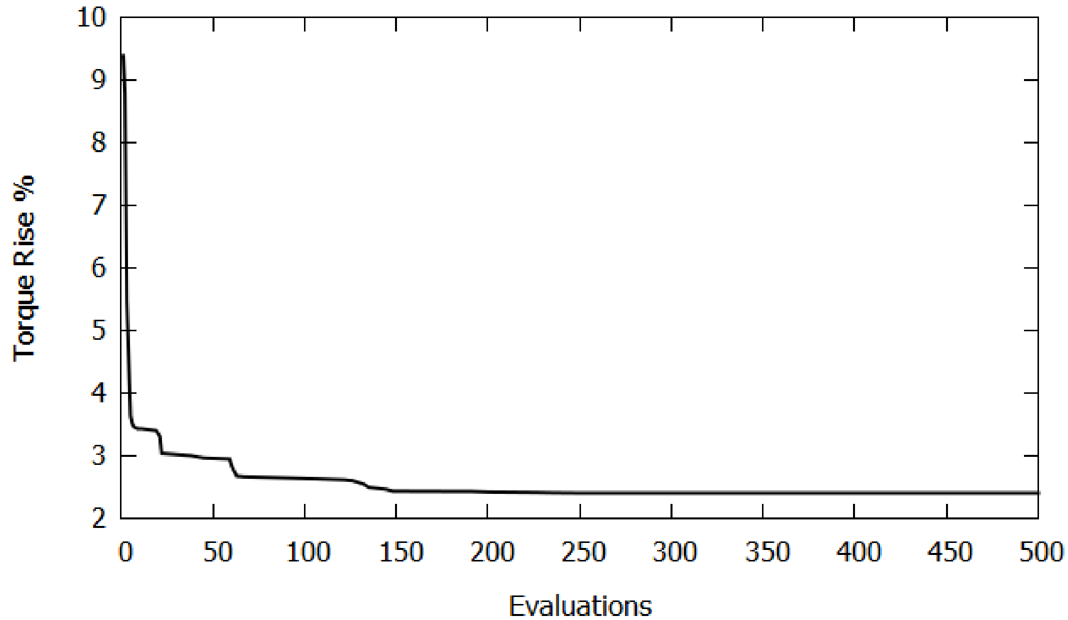

Figure 16: Case 4 final optimization run

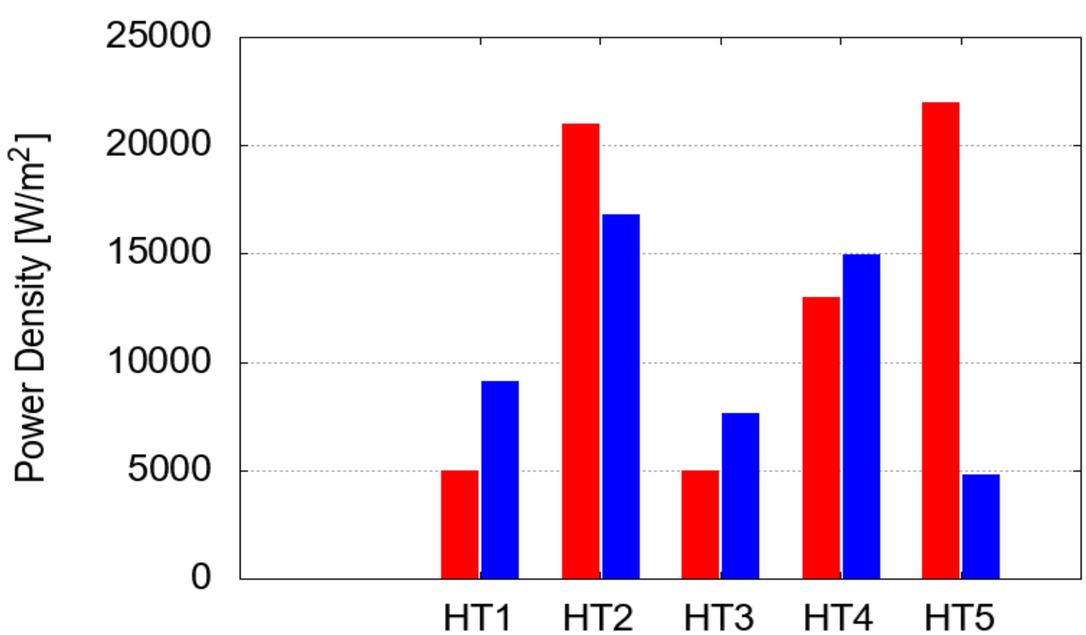

Figure 17: Case 4 initial (red) and optimized (blue) heating power

4.5.2 Periodic solution averaging

For unsteady stitching meshes, the initial flow, droplet and icing solutions are averaged over a cycle of one rotation for use on all subsequent CHT computations. To gauge the validity of this approximation, solution differences are computed for consecutive “averaged” solutions. In this case, 72 solutions constitute an averaged solution over a rotation as each solution is marched forward by a time corresponding to a timestep of 5 degrees of rotation. The first averaged solution contains solutions 1 to 72, representing the initial 360 degrees of rotation. The last solution averages the values in the flow fields of the rotation from 1635 to 1975 degrees and is used as the initial solution for all snapshots. A total of 395 averaged solutions are generated, and the normalized root mean squared difference for each consecutive pair is calculated for the pressure field (Figure 18) and density field in (Figure 19). The observed behaviour for both quantities shows the difference plummeting over the first two rotations before a plateau is established at 10^{-4} for density and 10^{-6} for pressure. This indicates that consecutive averaged solutions change less and less as more rotations are performed, demonstrating the validity of solution averaging.

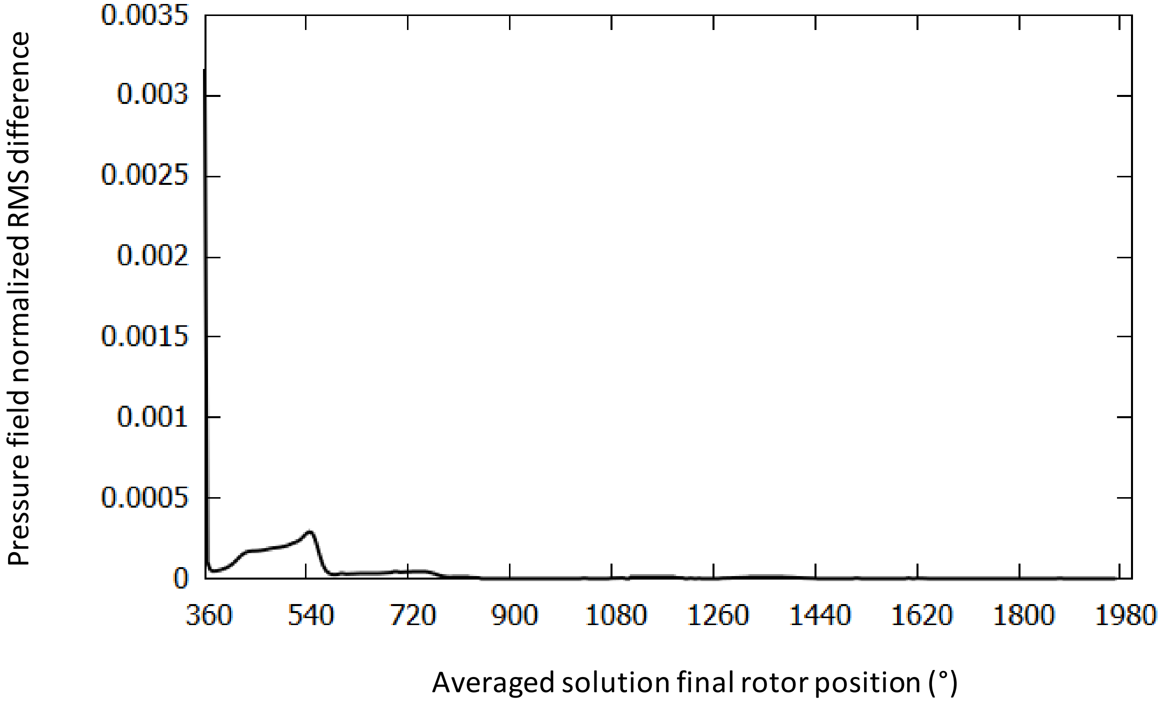

Figure 18: Pressure field normalized RMS difference for averaged solutions

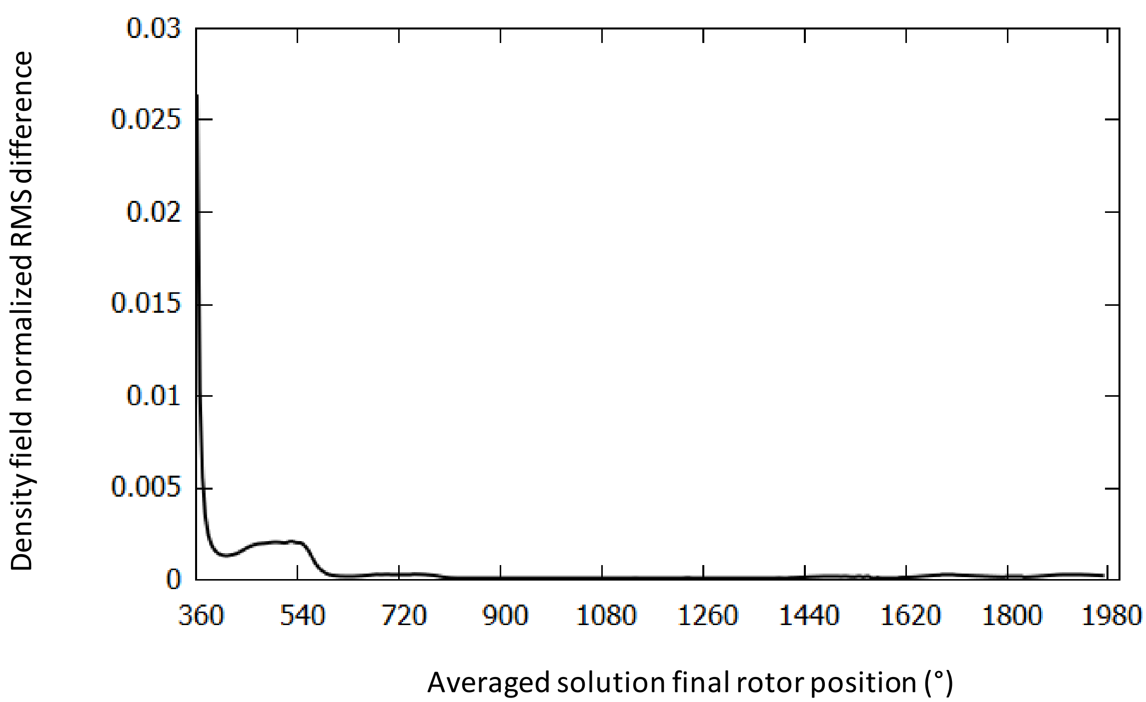

Figure 19: Density field normalized RMS difference for averaged solutions

4.6 Error analysis

LOOCV is conducted to gauge the extent of the error of the presented cases. Table 11 shows the LOOCV error analysis for the different models. Evidently, the ice accretion case suffers from the highest average error and maximum error and will be the subject of most improvement attempts throughout this section.

	Case 1	Case 2	Case 3	Case 4
Average Error	8.90%	0.35%	0.9%	0.8%
Max Error	25.9%	1.02%	3.07%	5.7%

Table 11: LOOCV error for all cases

4.6.1 Uniform sampling

Table 12 shows the effect of the addition of snapshots within the design space. However, model accuracy was not improved. Factors such as high non-linearity in the design space, a large number of design variables may accentuate the presence of high error regions. Many additional snapshots (hundreds or thousands) may need to be evaluated to attain a significant error reduction in a DoE with five design variables.

Snapshots (Uniform)	50	60	70	80
Average Error	8.90%	9.90%	9.60%	10.3%
Max Error	25.9%	27.9%	31.3%	31.5%

Table 12: Case 1 LOOCV error with addition of uniformly sampled snapshots

4.6.2 Localization

Localization error analysis is performed on the models in Table 12 by, at every snapshot, building a model with only the 30 "nearest" snapshots (excluding the current one). Then, a LOOCV is performed and the average (over the 30 errors) is retained. These averages are then averaged for all snapshots (50, 60, 70 or 80) of the model and are shown in Table 13. By this metric, localization shows a corresponding improvement of the average error for every model.

Snapshots	**50**	**60**	**70**	**80**
Average Error	8.25%	9.17%	9.12%	9.64%

Table 13: Case 1 LOOCV error of Table 12 results with localization

4.6.3 CFD vector snapshots

This method is applied to Case 3, where the flow solution snapshots are used to build the metamodel and the pressure field is taken for LOOCV analysis. The resulting average error is 0.06% and the maximum error over the domain 0.1%. However computational time during the evaluation of metamodel is significantly increased, rising from (1 to 3) seconds per iteration (for scalar variables) to approximately 10 minutes for flow fields. While it is a shorter time than the 2 hours needed for the direct computation of an aerodynamic solution, the timescale is infeasible for hundreds of optimization iterations.

4.6.4 Error-driven sampling

The error-driven sampling tool was utilized on the icing minimization problem, showing a reduction in the error in Table 14. 10 snapshots have been added at a time between refinement steps and the error threshold for refinement was 70%. As such, the refinement region contains the highest 30% of points ranked by their LOOCV error. This strategy yields the best results so far, with an acceptable additional computational cost expended prior to the optimization process.

Snapshots (Error-driven)	50	60	70	80
Average Error	8.90%	7.39%	7.12%	7.08%
Max Error	25.9%	18.5%	18.0%	17.5%

Table 14: Case 1 LOOCV error with error-driven addition of snapshots

4.7 Discussion

Results show that the optimization framework is effective at addressing all four studied problem formulations. As such, feasible sets of design variables which yield improving objective function values are found within a few hundred optimization iterations. In all cases presented, the IPS cannot maintain the surface ice-free, these problem formulations were chosen for two reasons. First, an IPS capable of maintaining an uncontaminated (ice-free) rotor above a power threshold is a more trivial case, limiting the potential of the research. Second, as Case 1 demonstrates, it shows that minimizing ice accretion is not necessarily equivalent to minimizing the aerodynamic impact. Indeed, engineering judgement must be exercised by the user as a choice must be made between seeking an uncontaminated surface and mitigating the aerodynamic impact in the case of an IPS unable to prevent ice accretion.

The developed framework addresses three dimensional rotorcraft icing flows, with highly nonlinear and a-priori unclear relationships between design variables and objective or constraint functions. Thus, results are expected to be entirely dependent on the studied case as an optimization problem for a different rotorcraft and flow conditions could yield very different results. Hence, it is difficult to draw universal conclusions about IPS design from specific studied cases. However, two general icing phenomena drive the aerodynamic impact and both are observed in the results. First, ice impingement occurs around the leading edge and is thus the location with highest amount of ice accretion if left unprotected. This prompts the optimizers to divert heating power towards the front of the blade (Cases 1, 3 and 4) in the quest of melting the incoming ice. The second effect is runback ice melted by the IPS that refreezes aft of the leading edge. If this occurs, the ice forming downstream on the chord can also cause aerodynamic degradation, which prompts the optimizer to extend the protection zone (Case 3) and the power of aft heaters (Case 2).

Error analysis was performed with Cases 2, 3 and 4 showing the average LOOCV error to be less than 1%, while Case 1 presents a higher average error (8.9%). While the error can be substantially reduced by using vector solutions of the entire CFD field as shown in Section 4.6.3, interpolating these fields during an optimization run is too time-consuming. Furthermore, adding uniformly sampled snapshots worsens the error. Comparing the average error in Tables 12 and 13, this is partially mitigated by using localization as it reduces the number of snapshots to create a metamodel. However, increasing the overall number of snapshots while using localization continues the error increase. Thus, error-driven sampling is used to judiciously distribute additional samples and reduce the LOOCV error. It must be noted that Case 1 uses the maximum ice accretion rate as its objective function, which only considers a single “worst point” and not the entire icing field. This leads to high variation and thus high error. Hence, although computationally efficient, this value yields limited-use results (Case 1) and therefore should only be used when the optimization problem seeks to obtain an uncontaminated surface.

5 Conclusions

A mathematically-based framework for optimizing electrothermal ice protection systems for helicopter rotors has been developed by combining a physics solver, helicopter tools, ROM and an optimizer. The research yields a modular design tool that allows the user to customize the optimization problem formulation with a palette of objective functions, design variables and constraints.

Outlined results demonstrate the capability of the framework to optimize the heating power and the heater extent design variables for both rotational frame of reference and stitching meshes, enabling support for any rotorcraft configuration and flow condition. Furthermore, in response to an odd case of counterproductive optimization results from minimizing the maximum ice accretion rate, aerodynamic objective functions and constraints are implemented. Thus, optimization results using torque rise as an objective function or constraint are obtained. However, they average a CFD simulation time of two hours per snapshot for relative frame of reference computations. As such, the framework is made cost-effective by taking advantage of ROM to create a metamodel from the results of high-fidelity CFD computations run a-priori and simultaneously to evaluate optimization iterations. Nevertheless, a concern for the metamodel accuracy arises from such an approach. Therefore, LOOCV is performed and a set of four error improvement strategies are implemented and their effectiveness is successfully analyzed.

Finally, the tool complements the McGill CFD Lab's helicopter analysis framework which supports computations of rotorcraft flow, icing, fluid-structure interaction, ice shedding and tracking.

6 References

[1] Beaugendre, H., Morency, F. and Habashi, W.G. "Development of a Second Generation In-flight Icing Code", *ASME Journal of Fluids Engineering*, vol. 128, no. 2, pp. 378-387, 2006.

[2] Werner, J. B. "Ice Protection Investigation for Advanced Rotary-Wing Aircraft", Lockheed-California CO Burbank, no. LR-25327-10, 1973.

[3] Van der Linden, F.R. and Seely, V.J. "The Boeing 247: the first modern airliner", University of Washington Press, 2011.

[4] Zumwalt, G., Schrag, R., Bernhart, W. and Friedberg R. "Electro-impulse de-icing testing analysis and design", NASA Contractor Report 4175, 1988.

[5] Goraj, Z. "An overview of the deicing and anti-icing technologies with prospects for the future", *24th international congress of the aeronautical sciences*, vol. 29, 2004.

[6] Overmeyer, A., Palacios, J. and Smith, E. "Ultrasonic de-icing bondline design and rotor ice testing", *AIAA journal*, vol. 51, no. 12, pp. 2965-2976, 2013.

[7] Palacios, J., Wolfe, D., Bailey, M. and Szefi, J. "Ice testing of a centrifugally powered pneumatic deicing system for helicopter rotor blades", *Journal of the American Helicopter Society*, vol. 60, no.3, pp. 1-12, 2015.

[8] Peterson, A.A. and Dadone, L.U. "Helicopter Icing Review", Boeing Vertol CO Philadelphia PA, no. D210-11583-1, 1980.

[9] Huang, X., Tepylo, N., Pommier-Budinger, V., Budinger, M., Bonaccurso, E., Villedieu, P. and Bennani, L. “A survey of icephobic coatings and their potential use in a hybrid coating/active ice protection system for aerospace applications”, *Progress in Aerospace Sciences*, vol. 105, pp. 74-97, 2019.

[10] Flemming, R.J. “A history of ice protection system development at Sikorsky Aircraft”, *FAA In-flight Icing / Ground De-icing International Conference & Exhibition*, SAE Technical Paper no. 2003-01-2092, 2003.

[11] Sinnett, M. “787 No-bleed systems: saving fuel and enhancing operational efficiencies”, *Boeing Commercial AERO magazine*, vol. 4, no. 1, pp. 6-11, 2007.

[12] Narducci, R. and Kreeger, R. E. "Analysis of a Hovering Rotor in Icing Conditions", NASA Technical Memorandum 2012-217126, 2012.

[13] Narducci, R., Orr, S. and Kreeger, R. E. "Application of a High-Fidelity Icing Analysis Method to a Model-Scale Rotor in Forward Flight", NASA Technical Memorandum 2012-217122, 2012.

[14] Kreeger, R. E., Sankar, L., Narducci, R. and Kunz, R. "Progress in Rotorcraft Icing Computational Tool Development", SAE Technical Paper no. 2015-01-2088, 2015.

[15] “Design of next-generation rotorcraft systems”, Siemens Product Lifecycle Management, http://mdx2.plm.automation.siemens.com/sites/default/files/flier/pdf/Rotorcraft_Tech.pdf, Accessed: 19 March 2021.

[16] Pellissier, M., Habashi, W.G. and Pueyo, A. “Design optimization of hot-air anti-icing systems by FENSAP-ICE”, *48th AIAA Aerospace Sciences Meeting Including the New Horizons Forum and Aerospace Exposition*, AIAA 2010-1238, 2010.

[17] Pourbagian, M. and Habashi, W.G. “Aero-Thermal Optimization of In-Flight Electro-Thermal Ice Protection Systems in Transient De-Icing Mode”, *International Journal of Heat & Fluid Flow*, vol. 54, no. 1, pp. 167-182, 2015.

[18] Pourbagian, M., Talgorn, B., Habashi, W.G., Kokkalaras, M. and Le Digabel, S. “Constrained Problem Formulations for Power Optimization of Aircraft Electro-Thermal Anti-Icing Systems”, *Journal of Optimization and Engineering*, vol. 16, no. 4, pp. 663-693, 2015.

[19] Le Digabel, S. “Algorithm 909: NOMAD: Nonlinear optimization with the MADS algorithm”, *ACM Transactions on Mathematical Software*, vol. 37, no. 4, pp. 1-15, 2011.

[20] Chen, L., Zhang, Y. and Wu, Q. “Heat transfer optimization and experimental validation of anti-icing component for helicopter rotor”, *Applied Thermal Engineering*, vol. 127, pp. 662-670, 2017.

[21] Khurram, R. A., Zhang, Y. and Habashi, W. G. “Multiscale finite element method applied to the Spalart–Allmaras turbulence model for 3D detached-eddy simulation”, *Computer Methods in Applied Mechanics and Engineering*, vol. 233, no. 1, pp. 180-193, 2012.

[22] Croce, G., Beaugendre, H. and Habashi, W.G. “CHT3D-FENSAP-ICE conjugate heat transfer computations with droplet impingement and runback effects”, *40th AIAA Aerospace Sciences Meeting & Exhibit*, AIAA 2002-0386, 2002.

[23] Fossati, M., Khurram, R.A. and Habashi, W.G. “An ALE mesh movement scheme for long-term in-flight ice accretion”, *International Journal for Numerical Methods in Fluids*, vol. 68, no. 8, pp. 958-976, 2012.

[24] Pendenza, A., Habashi, W.G. and Fossati, M. "A 3D mesh deformation technique for irregular in-flight ice accretion", *International Journal for Numerical Methods in Fluids*, vol. 79, no. 5, pp. 215-242, 2015.

[25] Nathoo, M., Habashi, W.G. and Fossati, M. "Stitching and Deformation of Non-overlapping Meshes for Unsteady Rotorcraft Aerodynamics*", 55th AIAA Aerospace Sciences Meeting,* AIAA Paper 2017-0582, 2017.

[26] Spalart, Ph.R. and Allmaras, S.R. "A One-Equation Turbulence Model for Aerodynamic Flows", *30th aerospace sciences meeting and exhibit*, p. 439, 1992.

[27] Gresho, P. M., Lee, R. L., Sani, R. L., Maslanik, M. K. and Eaton, B. E. "The Consistent Galerkin FEM for Computing Derived Boundary Quantities in Thermal and/or Fluid Problems", *International Journal for Numerical Methodsin Fluids*, vol. 7, no. 4, 1987.

[28] Messinger, B. L. "Equilibrium Temperature of an Unheated Icing Surface as a Function of Air Speed", *Journal of the Aeronautical Sciences*, vol. 20, pp. 29-42, 1953.

[29] Beaugendre, H., Morency, F. and Habashi, W.G. "FENSAP-ICE's three-dimensional in-flight ice accretion module: ICE3D", *Journal of aircraft*, vol. 40, no. 2, pp. 239-247, 2003.

[30] Statnikov, R. B. and Matusov, J. B. "Multicriteria optimization and engineering", Chapman & Hall, New York, 1995.

[31] Pourbagian, M. and Habashi, W. G. "Surrogate-Based Optimization of Electrothermal Wing Anti-Icing Systems", *Journal of Aircraft*, vol. 50, no. 5, pp. 1555-1563, 2013.

[32] Sobol, I. M. and Statnikov, R. B. "The choice of optimal parameters in multicriteria problems", Nauka (in Russian), Moscow, 1981.

[33] Zhan, Z., Habashi, W. G. and Fossati, M. “Real-Time Regional Jet Comprehensive Aeroicing Analysis via Reduced-Order Modeling”, *AIAA Journal*, vol. 54, no. 12, pp. 3787-3802, 2016.

[34] Du, Q., Faber, V. and Gunzburger, M. "Centroidal Voronoi Tessellations: Applications and Algorithms", *SIAM Review*, vol. 41, no. 4, pp. 637-676, 1999.

[35] Pourbagian, M. “Multidisciplinary Optimization of In-Flight Electro-Thermal Ice Protection Systems”, PhD Thesis, McGill University, 2014.

[36] Sirovich, L. “Turbulence and the Dynamics of Coherent Structures. Part I: Coherent Structures”, *Quarterly of Applied Mathematics*, vol. 45, no. 3, pp. 561-571, 1987.

[37] Jones, D. R. "A Taxonomy of Global Optimization Methods Based on Response Surfaces", *Journal of Global Optimization*, vol. 21, no. 4, pp. 345-383, 2001.

[38] Lappo, V. "Real-Time Aero-Icing Simulations Using Reduced Order Models," Master’s Thesis, McGill University, 2010.

[39] Zhan, Z. "Towards Real-Time CFD Simulation of In-Flight Icing", PhD Thesis, McGill University, 2016.

[40] Audet, C. and Dennis Jr, J.E. “Mesh adaptive direct search algorithms for constrained optimization”, *SIAM Journal on Optimization*, vol. 17, no. 1, pp. 188-217, 2006.

[41] Talgorn, B., Le Digabel, S., Kokkolaras, M., Pourbagian, M. and Habashi, W.G. "Optimization of an Aircraft Anti-Icing System Using Statistical Surrogates and Direct Search", CORS/INFORMS International Conference, Montreal, Canada, June 2015.

[42] Conn, A.R. and Le Digabel, S. “Use of quadratic models with mesh-adaptive direct search for constrained black box optimization”, *Optimization Methods and Software*, vol. 28, no. 1, pp. 139-158, 2013.

[43] Clarke, F. H. “Optimization and nonsmooth analysis”, John Wiley & Sons, New York, 1983.

[44] Zhan, Z., Habashi, W.G. and Fossati, M. “Local reduced-order modeling and iterative sampling for parametric analyses of aero-icing problems”, *AIAA Journal*, vol. 53, no.8, pp. 2174-2185, 2015.

[45] Caradonna, F.X. and Tung, C. “Experimental and Analytical Studies of a Model Helicopter Rotor in Hover”, NASA Technical Memorandum 81232, 1981.

[46] Brouwers, E.W. “The Experimental Investigation of a Rotor Icing Model with Shedding”, Master’s Thesis, Pennsylvania State University, 2010.

[47] Yassin, M. “Modelling of Iced Rotor Dynamics via CFD/CSD Coupling”, Master’s Thesis, McGill University, 2019.